

Design und Charakterisierung von lasergeschriebenen Mikrostrukturen zur effizienten Lichtsammlung

**Design and Characterisation of Light
Collecting Microstructures Fabricated by
Direct Laser-Writing**

Masterarbeit

ZUR ERLANGUNG DES AKADEMISCHEN GRADES
MASTER OF SCIENCE (M.Sc.)

IM STUDIENFACH PHYSIK

AM INSTITUT FÜR PHYSIK
DER MATHEMATISCHE-NATURWISSENSCHAFTLICHEN FAKULTÄT I
DER HUMBOLDT-UNIVERSITÄT ZU BERLIN

VORGELEGT VON

TANJA BIRGIT NEUMER

MATRIKELNUMMER: 541600

GUTACHTER:

1. Herr Prof. Dr. Oliver Benson
2. Herr Prof. Dr. Kurt Busch

Contents

1. Introduction	1
2. Fundamentals	5
2.1. Second Order Correlation Function	5
2.2. Nitrogen Vacancy Centre in Diamonds	8
2.2.1. General	8
2.2.2. Structural Properties	8
2.2.3. Optical Properties	9
2.2.4. Extracting Photons from Diamond	10
2.3. Three-Level System	11
2.4. Optical System/Tool Box	14
2.4.1. Spin Coating	15
2.4.2. Direct Laser-Writing	15
2.4.3. Electron Beam Physical Vapour Deposition	16
3. Optical Equipment	17
3.1. Experimental Methods	17
3.1.1. Scanning Confocal Optical Microscopy	17
3.1.2. Hanbury Brown and Twiss Setup	18
3.1.3. Back Focal Plane Imaging	19
3.2. Experimental Setup	20
3.2.1. Hanbury Brown and Twiss Setup	22
3.2.2. Back Focal Plane Imaging	22
3.2.3. Spectral Analysis	22
4. Measurements	25
4.1. Parabolic Micro-Antenna	25
4.1.1. Fabrication Process	26
4.1.2. Characterisation of the NDs	28
4.1.2.1. Alignment	28

Contents

4.1.2.2. Second Order Correlation Function	31
4.1.3. Saturation Intensity and Rate	32
4.1.4. Back Focal Plane Imaging	36
4.2. Photo-Resist	38
4.2.1. Fluorescence Measurement	38
4.2.2. Spectra	40
5. Modified Solid Immersion Lenses – Finite-Difference Time-Domain Calculations	43
5.1. The Finite-Domain Time-Differential Method	43
5.2. Modified Solid Immersion Lenses	45
5.2.1. Concept	45
5.2.2. Geometry	46
5.3. Simulation Settings	47
5.4. Results of the FDTD Simulations	49
5.4.1. Radiated dipole power	49
5.4.2. Light Collection Properties	49
5.4.3. Mode profile	51
6. Conclusion	55
A. Non-Linearity Correction	57

List of Figures

2.1.	Photon statistics for different light generation processes.	7
2.2.	Nitrogen vacancy centre in diamond: (a) crystallographic model. (b) photo-luminescence spectrum.	9
2.3.	Total internal reflection of nitrogen vacancy centres in bulk diamond.	11
2.4.	Scheme of a three-level system.	12
2.5.	Three-level system: (a) saturation rate. (b) second order correlation function.	13
2.6.	Schematic workflow of the DLW technique.	16
3.1.	Scheme of confocal microscope setup.	18
3.2.	Scheme of a Hanbury Brown and Twiss setup.	19
3.3.	Principle of back focal plane imaging.	20
3.4.	Basic scheme of experimental setup.	21
4.1.	Scheme of fabricated parabolic antenna.	26
4.2.	Darkfield microscopy image of a marker grid.	27
4.3.	Parabolic microstructure: (a) optical dark field image. (b) scanning electron microscope image.	28
4.4.	Two-dimensional plot of misalignments occurred after the fabrication process.	29
4.5.	Second order correlation measurement of an exemplary nitrogen vacancy centre.	31
4.6.	Saturation behaviour of an exemplary nitrogen vacancy centre (a) before and (b,c) after the fabrication process.	34
4.7.	Confocal and back focal plane images of a parabolic mirror with a ND in its focus.	37
4.8.	Confocal and back focal plane images of a parabolic mirror with randomly distributed NDs.	37
4.9.	Temporal behaviour of photo-resists.	39

List of Figures

4.10. Spectra of photo-resists.	40
5.1. Illustration of the spheroidal geometry of modified solid immersion lenses	46
5.2. Angular far-field intensity distributions for a standard SIL and two exemplary mSILs	50
5.3. Collection efficiency of a mSIL	51
5.4. Collection efficiency of the best mSILs	52
5.5. Best coupling efficiency between the mSIL's far-field and a Gaussian shaped fibre mode in dependence of the numerical aperture	53
5.6. Laser-written modified solid immersion lenses	54
A.1. Non-linear behaviour of the detection system.	58
A.2. Calibration curve for the count rate	59

List of Abbreviations

3D	three-dimensional
APD	avalanche photodiode
BFPI	back focal plane imaging
BS	beam splitter
CCD	charge-coupled device
CG	colour glass
cw	continuous wave
DETC	O,O-diethyl chlorothiophosphate
DLW	direct laser-writing
DM	dichroic mirror
EBPVD	electron beam physical vapour deposition
EMCCD	electron multiplier charge-coupled device
f	focal length
FDTD	finite-difference time-domain
FT	Fourier transform
HBT	Hanbury Brown and Twiss
HUB	Humboldt Universität zu Berlin
KIT	Karlsruher Institut für Technologie
L	lens
LP	longpass filter
LSB	lens system for back focal plane imaging
LSS	lens system for spectral analyse
M	mirror
MF	mirror on flip mount
mSIL	modified solid immersion lens
NA	numerical aperture
ND	nanodiamond
NFTFF	near-field to far-field transformation
NV	nitrogen vacancy

List of Abbreviations

NV⁻	negative charged nitrogen vacancy
NV⁰	neutral nitrogen vacancy
PD	photodiode
PETA	pentaerythritol triacrylate
PH	pinhole
PHF	pinhole on flip mount
PI	photo-initiator
PML	perfectly matched layer
PR	photo-resist
SEM	scanning electron microscope
SF	spatial filter
SIL	solid immersion lens
TCSPC	time-correlated single-photon counting
TIR	total internal reflection
ZPL	zero phonon line
a.u.	arbitrary units
cps	counts per second
m	meter
μ	micro
min	minutes
n	nano
s	second

1. Introduction

Many applications for quantum technologies such as secure quantum communication [1], quantum computation [2], and quantum sensing [3,4] require sources emitting only one single photon per excitation. In recent years, considerable efforts have been made displaying promising schemes and demonstrations for single-photon generation [5–7], like parametric down conversion using non-linear crystals [8], trapped ions and atoms [9, 10], single molecules [11], quantum dots [12, 13], and carbon nanotubes [14]. For practical applications sources are needed which can be implemented easily in existing networks. Thus, stable solid-state photon sources at room-temperature are favoured for the ease of integration [15]. The nitrogen vacancy (**NV**) centre in diamond is a promising candidate [16], ideally suited for use in quantum hybrid devices [17].

In general, extracting and detecting light from diamond is difficult. Especially in bulk diamonds, total internal reflection at the medium-air interface restricts the efficient outcoupling of light due to the diamonds' high refractive index. To overcome this problem, the use of nanometre sized diamond crystals, so called nanodiamonds, has become common as they represent point-like emitters.

There are mainly two issues concerning the efficient light extraction: the quantum yield and the omni-directional emission of the **NV** centre. The quantum yield in terms of collecting single-photon emitters quantifies how efficient the source emits a photon after the system has been excited. In the ideal case the quantum yield is equal to one, i.e. at any time the quantum source is excited a photon is emitted in return. In order to increase the quantum yield, the Purcell effect can be exploited which states that the spontaneous emission can be modified resonantly by placing the emitter in an optical cavity [18–20] or in a plasmonic structure [21]. By enhancing the **NV**'s radiative emission the non-radiative decay channels are suppressed. The aspect of omni-directional emission can be countered using 4π detection optics. However, this is impractical for almost all applications, which leaves the option to modify the direction of the emitted photons. This alteration of the emission distribution can be achieved by using resonant structures, such as mentioned above, or by the

1. Introduction

placing a nanodiamond onto an optical fibre without additional optical elements [22]. Alternatively, geometrical optics can be employed [23].

In this thesis, the collection efficiency of photons is enhanced by altering the direction of the photons only. We use a geometrical approach to engineer the angular radiation distribution of the NV centre so that photons are directed into solid angles as small as possible. Hence, the need for high numerical aperture optics is not given any longer. We exploit light refraction and constraints imposed by total internal reflection to control the radiation distribution of light in terms of limiting the light's propagation into a small numerical aperture. However, the potential of our approach is not limited to the enhancement of the light collection but also to tailor the light's mode profile which enables for efficient fibre coupling.

The foundation of our geometrical approach is the feasibility of fabricating micrometre sized structures by means of the direct laser-writing method [24]. This technique uses a focussed femtosecond laser pulse to polymerise a photo-resist in a non-linear process only at the laser's focus. Microstructures of nearly arbitrary three-dimensional shape can be produced. Using photostable single-photon emitters, like NV centres, offers the ability to incorporate them in the structures already during fabrication [25].

Using this method, we show the fabrication of parabolic micro-antennas at the positions of pre-selected nitrogen vacancy centres in nanodiamonds in an aligned process. We identify the problems in the alignment procedure and execute measurements prior and after the structure's fabrication. While the incorporation of the NV centre in the photo-resist is possible, its detection during the DLW process is more difficult. Thus, the fluorescence of different photo-resists, exposed and unexposed, is investigated to indicate their capability to allow the detection nitrogen vacancy centres' fluorescence during the laser-writing process.

Additionally we analyse a second geometrical architecture. By depositing nanodiamonds containing single nitrogen vacancy centres directly onto a solid immersion lens made of ZrO₂, the highest count rate observed for a single nitrogen vacancy centre has been reported to be 853×10^3 cps [26]. Based on the concept of solid immersion lenses, we investigate the light collecting properties of lenses in form of truncated spheroids using finite-domain time-difference calculations.

The thesis' is structured as described below.

Chapter 2 gives basic information of single-photon emission and the quantum source employed – the nitrogen-vacancy centre in diamond. In addition, the theoretical emission characteristics of a three-level system are presented which exhibits a

simplified model for the nitrogen vacancy centre. Finally, different methods applicable to fabricate light collecting architectures are discussed.

Chapter 3 explains the experimental methods which are needed to address quantum emitters and characterise their photon emission properties as well as their angular emission distribution. In addition, their experimental implementation in our setup is described.

Chapter 4 contains the measurements to characterise the parabolic mirror fabrication and the results of the improved light collecting method.

Chapter 5 discusses a novel design for light collecting architectures using different spheroidal geometries, the so called modified solid immersion lenses. Their light collection properties are investigated in finite-domain time-differential calculations.

Chapter 6 gives the results obtained throughout this thesis. We conclude with an outlook on light collecting microstructures using laser-written structures – the possibilities for improvements, constraints in the geometrical approach and potential for further developments.

2. Fundamentals

In this chapter we give a short introduction to the theoretical background of single-photon emission. After presenting some general properties of the quantum light source used, that being the nitrogen vacancy centre in diamond, we discuss an appropriate model for the nitrogen vacancy centre emission characteristics, the three-level energy system [16]. Eventually a tool box of methods, those used to modify angular emission distribution, is presented.

2.1. Second Order Correlation Function

Single-photon emitters generate per definition only one photon per excitation cycle. In experiments, the process of light generation can be distinguished by measuring its photon statistics. The theoretical foundation, known as correlation functions, was introduced by Glauber in 1963 [27]. Therein, the statistical properties of electromagnetic fields and the dynamics of the light generation are studied theoretically.

In the following, a short overview of basic knowledge in terms of the quantization of radiation is presented. Operators and vectors are marked using a hat ($\hat{\cdot}$) and bold letters, respectively.

The electromagnetic field can be expressed in terms of the bosonic annihilation and creation operator, \hat{a} and \hat{a}^\dagger , respectively [28]. The commutation relation of the annihilation and creation operators is given by $[\hat{a}, \hat{a}^\dagger] = 1$. The quantized electric field $\hat{\mathbf{E}}$ with j modes, takes the form

$$\hat{\mathbf{E}}(\mathbf{r}, t) = \sum_j i \sqrt{\frac{\hbar \omega_j}{2\epsilon_0 V_j}} [\epsilon_k \hat{a}_k e^{i(\mathbf{k}\mathbf{r} - \omega_j t)} + \epsilon_k \hat{a}_k^\dagger e^{-i(\mathbf{k}\mathbf{r} - \omega_j t)}] \quad (2.1)$$

$$= \hat{\mathbf{E}}^{(-)} + \hat{\mathbf{E}}^{(+)}, \quad (2.2)$$

with t being the time, \mathbf{r} , \mathbf{k} , and ϵ_k , being space, wave, and polarization vector, respectively. The frequency ω_j and volume V_j correspond to the j th mode. The constants \hbar is the reduced Planck constant and ϵ_0 is the free space permittivity,

2. Fundamentals

respectively. The field operator can be separated in a positive and negative frequency term, where $\hat{\mathbf{E}}^{(-)}$ contains only the creation operators \hat{a}^\dagger and its adjoint $\hat{\mathbf{E}}^{(+)}$ contains only the annihilation operators \hat{a} .

In quantum optics, especially the second order correlation function is an indispensable tool to study non-classical features of light. This function quantifies, how the detection of one photon at time t from a light source influences the probability to detect another one at t' . Measuring the normalized second order correlation function $g^{(2)}$ allows us to verify if a source is a true single-photon emitter. The function $g^{(2)}$ is given by:

$$g^{(2)}(t; t') = \frac{\langle \hat{\mathbf{E}}^{(-)}(t) \hat{\mathbf{E}}^{(-)}(t') \hat{\mathbf{E}}^{(+)}(t) \hat{\mathbf{E}}^{(+)}(t') \rangle}{\langle \hat{\mathbf{E}}^{(-)}(t) E^{(+)}(t) \rangle \langle \hat{\mathbf{E}}^{(-)}(t') E^{(+)}(t') \rangle}, \quad (2.3)$$

where $\langle \dots \rangle$ denotes time averaging. For a continuous excitation of a single quantum emitter the ensemble averages are time independent. This means using the time difference τ we can replace t with $t = t' + \tau$. Furthermore, the starting time of the measurement can be chosen arbitrarily because we average over time t . Therefore, we set $t' = 0$ what leads to:

$$g^{(2)}(\tau) = \frac{\langle \hat{\mathbf{E}}^{(-)}(0) \hat{\mathbf{E}}^{(-)}(\tau) \hat{\mathbf{E}}^{(+)}(\tau) \hat{\mathbf{E}}^{(+)}(0) \rangle}{\langle \hat{\mathbf{E}}^{(-)}(0) \hat{\mathbf{E}}^{(+)}(0) \rangle^2}. \quad (2.4)$$

Random processes, such as light generation, are uncorrelated at long time scales. A consequence is that the correlation function $g^{(2)}$ approaches 1 on a time scale τ comparable to the coherence time of the light field [29].

Based on the second order correlation function at zero time delay $g^{(2)}(0)$ light states can be distinguished into the following cases (see also Figure 2.1):

- Bunched light: $g^{(2)}(0) > 1$
A value of $g^{(2)}(0) > 1$ denotes that the probability to detect a second photon immediately after a first event is increased. This light is produced by chaotic sources, e.g. a light bulb or a discharge lamp.
- Coherent light: $g^{(2)}(0) = 1$
A value of $g^{(2)}(0) = 1$ denotes that the probability to detect a second photon after a first event is independent on the detection of the first, which is described by a Poisson distribution. This light is produced by a laser far above threshold.

2.1. Second Order Correlation Function

- Anti-bunched light: $g^{(2)}(0) < 1$

A value of $g^{(2)}(0) < 1$ denotes that the probability to detect a second photon immediately after a first event is decreased. This light is produced by continuously driven single quantum sources.

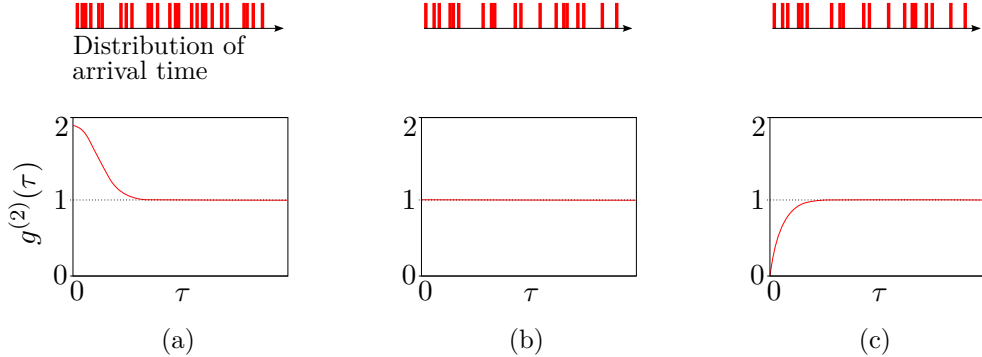


Figure 2.1.: Illustration of the photon arrival time and its corresponding second order coherence function $g^{(2)}(\tau)$ for different light states. (a) bunched light, (b) coherent light, (c) anti-bunched light. (Adapted from [30])

In the special case of a single mode electric field of frequency ω_0 with a well-defined photon number n the light represent Fock state [28]. The expectation value of a Fock state with $\langle \hat{n} \rangle$ photons is per definition $\langle \hat{n} \rangle = \hat{a}^\dagger \hat{a}$. Thus, we obtain the following expression for $g^{(2)}(0)$:

$$g^{(2)}(0) = \frac{\langle \hat{a}^\dagger \hat{a}^\dagger \hat{a} \hat{a} \rangle}{\langle \hat{a}^\dagger \hat{a} \rangle^2} = 1 - \frac{1}{n}. \quad (2.5)$$

As stated above, a true single-photon source generates only one photon in a single excitation cycle, hence the particle number is given by $n = 1$. This means the correlation function at zero time delay is $g^{(2)}(0) = 0$, which is referred to as anti-bunching dip. This is exactly the anti-bunching behaviour expected, verifying that the source is a true single-photon source.

This means a single nitrogen vacancy centre in nanodiamond has in the ideal case a vanishing second order correlation value at zero time delay. However, in experiments, background light and detectors' dark counts can reduce the effect of anti-bunching as they mimic additional sources. Thus, a experimental value of $g^{(2)}(0) < \frac{1}{2}$ indicates that the observed light stems predominantly from one single-photon emitter. This value is significant since two independent single emitters have in the ideal case value of $g^{(2)}(0) = \frac{1}{2}$.

2. Fundamentals

2.2. Nitrogen Vacancy Centre in Diamonds

After the ability of addressing a single nitrogen vacancy centre in diamond [31], it was soon demonstrated that it is a photo-stable solid-state source of single-photons at room-temperature [16]. This property renders the nitrogen vacancy centre very attractive for the implementation in quantum technology application.

In this section, we will give a short overview of those characteristics of the nitrogen vacancy centre, which are especially important for this work. A comprehensive review of the current knowledge about nitrogen vacancy centres can be obtained from [32].

2.2.1. General

Diamond itself, a semiconductor with a wide band gap of 5.5 eV [33], is transparent in the spectral range from the ultraviolet to the infrared [34], but vacancies or impurities existing in the diamond lattice lead to additional energy levels within the band gap, resulting in defects, known as colour centres. To date there have been more than 500 colour centres observed [15]. Among them, the nitrogen vacancy (**NV**) centre is the most studied defect centre in diamond.

NV centres are found in two different arrangements, in bulk diamond and nanocrystals as small as 5 nm [35], called nanodiamonds (**NDs**). A **ND** with a much size smaller than its emission wavelength can be approximated as point source emitting into free-space. Throughout this thesis **NDs** are the system of choice as single-photon emitters.

Henceforth we will refer to nanodiamonds containing one single nitrogen vacancy centre, simply as nanodiamonds . However, the number of **NV** centres in a nanodiamond can vary – **ND** can also possess more than one **NV** centre or none.

2.2.2. Structural Properties

The **NV** centre consists of a substitutional nitrogen atom adjacent to a vacancy in the diamond lattice [15], shown in Figure 2.2a. The defect exists in two optically active charged states, the neutral NV^0 [36] and a negatively charged NV^- [37]. Both charged states can be found within the same defect centre [38]. Clearly, the two states do not have the same electronic configuration, causing distinct optical and spin properties. Due to its non-vanishing intrinsic spin, only the negatively charged NV^- centre remains as a prominent candidate in quantum technology applications and spin manipulation experiments [37]. Other than single-photon fluorescence, the neutral

2.2. Nitrogen Vacancy Centre in Diamonds

NV^0 has not yet been employed for quantum optical experiments. Suggestions exists to utilize it as a spin qubit [39].

Owing to its enormous attention in scientific research, this thesis focus on the negatively charged NV^- centre in this thesis, referring to simply as NV centre.

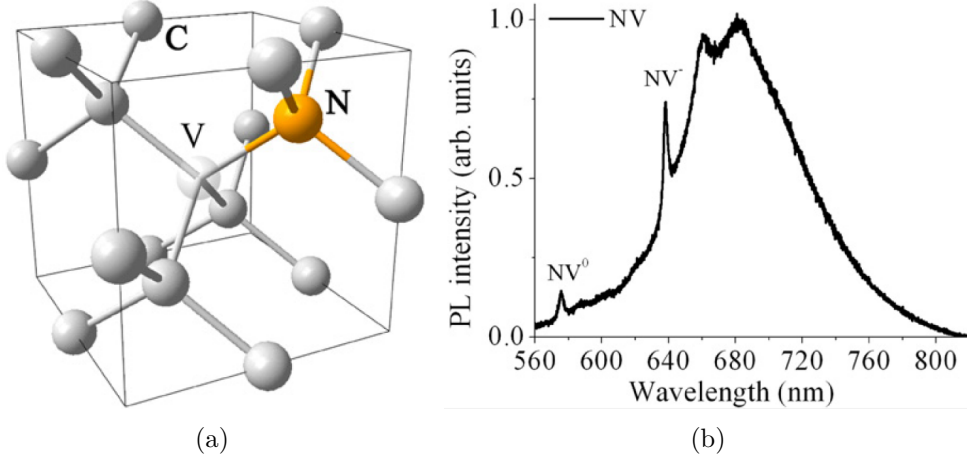


Figure 2.2.: (a) crystallographic model of the NV centre in diamond. (b) photoluminescence spectrum showing the ZPLs of the neutral (575 nm) and the negatively charged (637 nm) NV centre with the phonon side bands at room-temperature. (Taken from [15])

The exact energy level system of the NV^- centre is still under debate, but the latest results indicate a complex level structure with sub-levels of the excited and the metastable states [40–43]. However, photon statistics from a typical single NV^- centre show that the system's dynamic can be modelled as a standard three-level system [16].

2.2.3. Optical Properties

A characteristic feature of the NV centre's states are their zero phonon lines (ZPL), which are produced by optical transitions between purely electronic states. Transitions to electronic-phonon states create a broadened vibronic spectrum, the phonon side bands, around the ZPL. The phonon side bands enables for optically exciting the systems off-resonantly.

The NV^0 has its ZPL at 575 nm [44] with a broad phonon side band that extends from 580 nm to 650 nm [45], whereas the NV^- exhibits its ZPL at 637 nm [46] with a phonon side band extending to 800 nm [47], shown in Figure 2.2b. However, the ZPLs suffer from dynamic frequency fluctuations, referred to as spectral diffusion

2. Fundamentals

which is much more distinctive in NDs than in bulk diamond. Even at cryogenic temperatures, the ZPLs experience spectral diffusion resulting in a decreased degree of indistinguishability [48] which is drawback for the NVs' implementation in quantum application. However, the experiments throughout this thesis are not designed for the examination of their degree of distinguishability.

2.2.4. Extracting Photons from Diamond

Diamond imposes a constraint on the collection efficiency of photons due to high total-internal reflection (TIR) at the diamond-air interface. TIR occurs when light travels from a medium with a higher refractive index, diamond, to one with a lower refractive index, air with $n_{air} \approx 1$. Using Snell's law this appears at an critical angle of incident of $\theta_C = \arcsin(\frac{n_{air}}{n_{dia}}) \approx 24.6^\circ$ with the high refractive index of diamond being ($n_{dia} = 2.4$). The range of angles which are refracted to the objective is reduced to $2\theta_C$. Thus, instead of an solid angle of 2π for one hemisphere, only light can be collected in an effective solid angle of less than 0.2π . This is a reduction by a factor of 10. In combination with the limited numerical aperture of collecting optics, a great extent of generated photons is lost.

In microscopy, the numerical aperture (NA) of a system is used to measure its ability to gather light. It is defined by

$$NA = n \sin(\Phi), \quad (2.6)$$

with n being the refractive index of the objective's surroundings. The lens accepts only light entering in a certain solid angle of a cone. Φ is the half angle of the maximum cone of light that is accepted by the lens.

In bulk diamond, this results in typical count rates from single NV centres of around 40×10^3 cps (counts per second) [49] for collection efficiency between 1% and 2%.

There are geometric approaches to enhance the collection efficiency. One way is to combine the emitter with solid immersion lenses (SILs) yielding an increased efficiency of one order of magnitude [50–52]. Another possibility is using a combination of photonic nano-wires with confocal microscopy, at which the efficient coupling of NV photons to the strongly confined mode in the diamond nano-wire lead to the improvement [53].

On the other hand subwavelength-sized nanodiamonds act as point sources and hence avoid the loss of light caused by the diamond-air interface in bulk diamond.

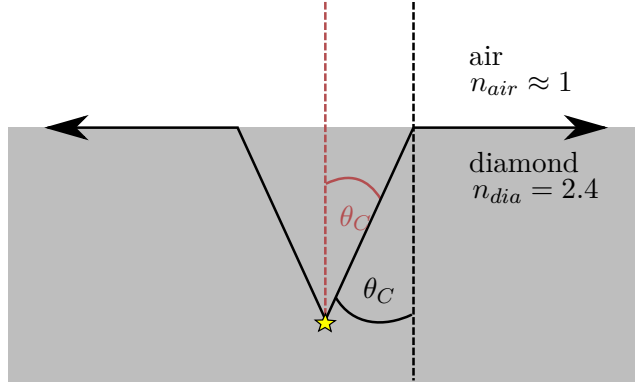


Figure 2.3.: Total internal reflection occurs for light travelling from a medium with higher refractive index, diamond, into a medium with a lower refractive index, air. At a critical angle of $\theta_C \approx 24.6^\circ$ light is not refracted into air but reflected at the air-diamond interface.

Thus, higher collection efficiencies are yielded. However, due to an increased excited-state lifetime in NDs compared to bulk diamond the emission rate is lower. Another constraint is the intrinsic quantum efficiency which is in the case of NVs in nanodiamonds widely distributed between 10% and 90% [54, 55]. This limits the maximal intrinsic emission rate. With a collection efficiency between 1% and 2%, the typical count rates from single NV centres in nano-crystal diamond are around 200×10^3 cps [56].

2.3. Three-Level System

The aim of this thesis is to enhance the light collection of single-photon sources using a geometrical approach. In order to do this, the exact electronic configuration of the source is not important wherefore a simplified energy level model can be employed. Neglecting the complex sub-level structure, a typical single NV⁻ centre can be described as a three-level system [16], shown in Figure 2.4.

In this section the intrinsic parameters of the nitrogen vacancy centre, such as its emission efficiency and second order correlation function, are discussed, dependent on this simplified three-level model following the textbook 'Principles of Nano-Optics' [57].

The transition rates of the system are indicated as k_{12} , k_{21} , k_{23} and k_{31} , whereas the transitions involving level three are assumed to be non-radiative. Using the

2. Fundamentals

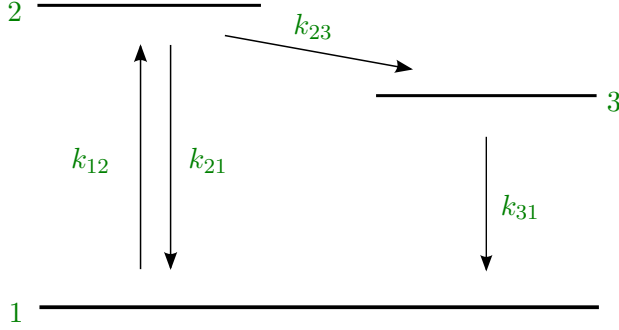


Figure 2.4.: Scheme of a simplified three-level system applied to model the emission dynamics of a NV^- centre.

population probability $p_i(t)$ of the levels $i = 1, 2$, and 3 , the dynamics of a three-level system can be expressed via its rate equations, as follows:

$$\frac{\partial p_1(t)}{\partial t} = -k_{12}p_1(t) + k_{21}p_2(t) + k_{31}p_3(t), \quad (2.7)$$

$$\frac{\partial p_2(t)}{\partial t} = k_{12}p_1(t) - (k_{21} + k_{23})p_2(t), \quad (2.8)$$

$$\frac{\partial p_3(t)}{\partial t} = k_{23}p_2(t) - k_{31}p_3(t), \quad (2.9)$$

$$1 = p_1(t) + p_2(t) + p_3(t), \quad (2.10)$$

where the additional constraint, Equation 2.10, is due to the conservation of population probability.

Emission Rate

We are interested in the power dependence of the emission rate R . R is given by the spontaneous emission rate k_{21} times the population of the excited state p_2 .

$$R = k_{21}p_2 \quad (2.11)$$

As a first step, the population of p_2 is derived. For a continuous wave excitation we can make the assumption that the system is in equilibrium ($t \rightarrow \infty$), hence all time derivatives are zero. The system of equations can be solved analytically, yielding

$$p_2(\infty) = \frac{k_{12}}{k_{12} + k_{21} + k_{23}\left(\frac{k_{12}}{k_{31}} + 1\right)}. \quad (2.12)$$

2.3. Three-Level System

The relation between absorption rate k_{12} and the average absorbed power $\langle P \rangle$ is given by $k_{12} = \frac{\langle P \rangle}{\hbar\omega_e}$ with the excitation frequency ω_e . Furthermore, $\langle P \rangle$ can be expressed by $\langle P \rangle = \sigma I$, with σ and I being the absorption cross section and the excitation intensity, respectively. Plugging the expressions for p_2 , k_{12} and $\langle P \rangle$ into Equation 2.11 yields to the function for R dependent on the excitation intensity I :

$$R(I) = R_\infty \frac{I/I_s}{1 + I/I_s}, \quad (2.13)$$

with

$$R_\infty = \frac{k_{31}k_{21}}{k_{23} + k_{k31}}, \quad (2.14)$$

$$I_s = \frac{(k_{21} + k_{23})k_{31}}{k_{23} + k_{k31}} \frac{\hbar\omega_e}{\sigma}. \quad (2.15)$$

R_∞ is the maximal emission rate for infinite excitation intensities ($I \rightarrow \infty$) and I_s is the saturation intensity, i.e. the intensity at a emission rate of $R = \frac{R_\infty}{2}$. Equation 2.13 describes the saturation behaviour of the emission rate, illustrated in Figure 2.5a.

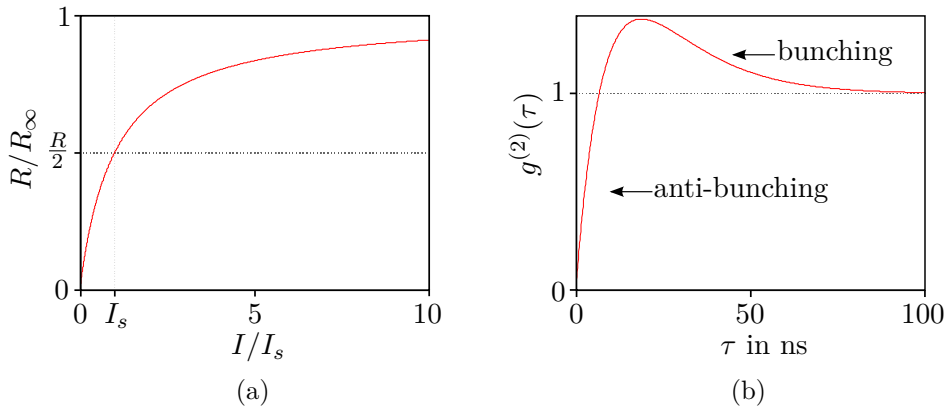


Figure 2.5.: Three-level system. Using equation 2.13, the theoretical behaviour of the saturation of the emission rate is shown in (a). A plot of the second order correlation function (Eq. 2.17) is depicted in (b) using the parameters: $c = 4$, $\tau_1 = 10$ ns and $\tau_2 = 15$ ns.

Second Order Correlation Function $g^{(2)}$

The second order correlation function $g^{(2)}(t)$ gives the probability to detect a second photon at the time $t + \tau$ after the arrival of the first photon at time t , normalised

2. Fundamentals

by the average photon detection rate (c.f. Section 2.1). Assuming the system to be excited continuously t can be set to zero ($t = 0$) which is no limitation for a stationary process. The probability to detect a photon at time τ after the initial photon is proportional to $\eta k_r p_2(\tau)$, with η as the detection efficiency of the system. The steady-state count rate p_2 (Eq. 2.12) measured after sufficiently long time ($t \rightarrow \infty$) is the normalisation factor of the coherence function $g^{(2)}$, given by $\eta k_r p_2(\infty)$. It follows:

$$g^{(2)}(\tau) = \frac{\eta k_{21} p_2(\tau)}{\eta k_{21} p_2(\infty)}. \quad (2.16)$$

With the initial condition of the emitter being in the ground state $p_1(t) = 1$, $p_2(t) = 0$, and $p_3(t) = 0$ the time-dependent solution for $p_2(\tau)$ can be derived [57], resulting in the following solution for $g^{(2)}$:

$$g^{(2)}(\tau) = 1 - (1 + c) \exp^{\tau/\tau_1} + c \cdot \exp^{\tau/\tau_2}, \quad (2.17)$$

with the decay times $\tau_{1,2}$ and coefficient c given by

$$\tau_{1,2} = \frac{2}{-A \pm \sqrt{A^2 - 4B}}, \quad (2.18)$$

$$c = \frac{\tau_2 + k_{31} - k_{12} \frac{k_{23}}{k_{31}}}{\tau_1 - \tau_2}, \quad (2.19)$$

$$A = k_{12} + k_{21} + k_{23} + k_{31}, \quad (2.20)$$

$$B = k_{23}(k_{12} + k_{31}) + k_{31}(k_{12} + k_{21}). \quad (2.21)$$

In Figure 2.5b the resulting curve is illustrated. Due to the lifetime of the metastable level being typically longer than the excited state lifetime, a bunching behaviour can be observed in addition to the characteristic anti-bunching dip at $\tau = 0$.

2.4. Optical System/Tool Box

The goal of this thesis is to optimise the emission directivity of a single NV centre using an approach relying purely on geometrical optics. Therefore, the light collecting properties of parabolic antennas (Sec. 4.1) and special non-spherical lenses (Sec. 5.2) are investigated. The incorporation of the emitter on a pre-defined location within these structures needs the use of different techniques, which are spin coating, direct laser-writing, and electron beam physical vapour deposition.

2.4. Optical System/Tool Box

In this section, we give a short overview of the basic principles of the fabrication and preparation methods.

2.4.1. Spin Coating

A crucial point in this thesis is addressing single colour centres. This means a technique is needed to isolate individual emitters. Since our **NDs** are stored in water solutions, spin coating represents a simple method to apply them.

Spin coating is a method to deposit uniform thin films of a solution on flat substrates, e.g. glass cover slides. The substrate rotates at high speed resulting in a homogeneous spread of the coating material due to centrifugal force. The desired particle density depends on the concentration of the **ND**/water solution, the angular speed of spinning and the duration of spinning. This procedure is done with a commercial spin coating machine.

2.4.2. Direct Laser-Writing

Direct laser-writing (**DLW**) is a rapid and cheap technique to fabricate essentially any arbitrary, complex, three-dimensional (**3D**) micro-structure. The workflow of the **DLW** method is depicted in Figure 2.6, starting with the photo-resist applied onto a glass substrate (Fig. 2.6a). In a conventional **DLW** process, a pulsed laser is focused into a small volume of photo-resist (Fig. 2.6b). The **PR** consists of a monomer and a photo-initiator (**PI**). The wavelength of the laser is chosen such, that it corresponds to approximately twice the wavelength of the one-photon absorption maximum of the **PI** and only two-photon absorption is possible. Only in the vicinity of the focal spot the intensity is sufficiently large to initiate significant two-photon absorption of the **PI** which decays into free radicals. These radicals initiate the polymerization of the monomer. Owing to the non-linear process, only a small **3D** volume is exposed. Thus, lateral linewidths down to below 100 nm routinely be produced [58]. Recently, resolutions beyond the classical diffraction limit have been achieved with an improved **DLW** method [58]. By scanning the sample with respect to the focal volume, the three-dimensional structure is fabricated (Fig. 2.6c). After the exposure is completed, the unexposed resist is dissolved during the development in a solvent bath and removed by rinsing the sample with acetone resulting in a free-standing three-dimensional microstructure (Fig. 2.6d).

2. Fundamentals

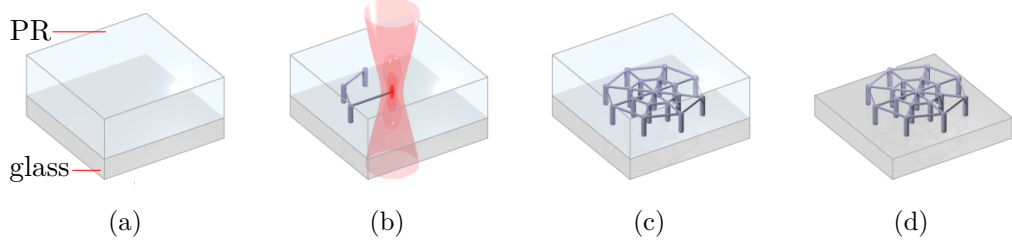


Figure 2.6.: Schematic workflow of the **DLW** technique. (a) after the photo-resist is dropcasted onto the glass substrate, (b) PR is exposed at the laser's focal spot. By moving the sample sample with respect to the laser's focus, (c) the exposed structure within the unexposed photo-resist is fabricated. (c) after removing the unexposed PR the free-standing 3D structure is obtained. (Adapted from [59])

In a collaboration with the Wegener Group, at the Karlsruhe Institute of Technology (**KIT**), the **3D** structures (parabolic antennas and special non-spherical lenses) were fabricated. Further information on their research can be found in [24, 58, 60].

2.4.3. Electron Beam Physical Vapour Deposition

Electron beam physical vapour deposition (**EBPVD**) is a method of depositing thin films by ejecting material from a target onto a substrate. Under high vacuum a thermionic cathode releases electrons which are accelerated using a high voltage electrode and directed with electromagnets to the target. Thus the energetic electron beam bombards the solid target material causing its atoms to enter the gaseous phase. The ejected (sputtered) atoms condensate and form a thin layer on the substrate. This allows to create homogeneous layers with thicknesses ranging from fractions of a nanometre to several micrometres.

This process produces high-purity, high-performance solid materials. The deposition materials used are silver (Ag) and magnesium fluoride (MgF_2).

3. Optical Equipment

This work deals with the ability to tailor the emission directivity of single nitrogen-vacancy centres in nanodiamonds embedded in laser-written structures. In order to compare the NV centres characteristics with and without the light collecting structure, different optical analysis methods are applied.

Since addressing and detection of single-photon sources needs, in addition to a high resolution also a high contrast, a scanning confocal microscope is used. Mainly three different characterisation methods are deployed. A Hanbury Brown and Twiss setup measures the second order correlation function $g^{(2)}(\tau)$ in order to verify single-photon statistics. Further, back focal plane imaging is used to investigate the angular radiation distribution and a spectrometer is deployed which gives information about undesirable fluorescence of the material used to build the structures.

In this chapter, the principles of the techniques used are given and subsequently a detailed description of experimental setup is presented.

3.1. Experimental Methods

3.1.1. Scanning Confocal Optical Microscopy

Confocal microscopy has two essential advantages compared to conventional wide field microscopy; those being the increased resolution, especially in the axial direction, and its highly improved signal to noise ratio [61]. The key of these improvements is the combination of a punctuate illumination and detection. This allows for detection of low photon rates, e.g. originating from single quantum emitters.

The principle of confocal microscopy is illustrated in Figure 3.1a. Light from a point source is shone at a single point of the object with a diffraction limited spot size. Thus, only a small volume of the sample is illuminated. Then, in turn, this spot is imaged on a pinhole. All these points are confocal. The effect of this spatial filtering is depicted in Figure 3.1b,-c,-d. Light originating from the focal spot of the objective is transmitted through the pinhole (Fig. 3.1b), while light from off-axis points (Fig. 3.1c) or points not in the focal plane (Fig. 3.1d) is mostly blocked by the

3. Optical Equipment

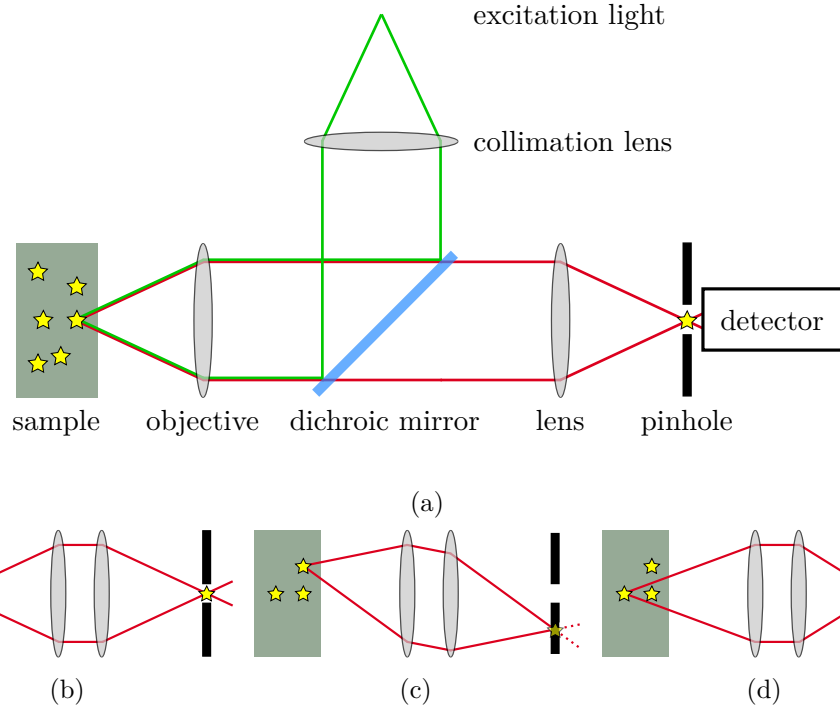


Figure 3.1.: (a) scheme of confocal microscope setup. The path of the excitation light is drawn green, the path of the detection light red. (b) light confocal with the detection pinhole is transmitted through the pinhole, whereas light from (c) off-axis points or (d) from points not originating from the focal plane are spatially filtered out.

pinhole. Thus, merely light stemming from the focal spot contributes to the detected signal and background is suppressed.

This confocal configuration has an intensity distribution in the object plane given by multiplying the point spread functions of the excitation point source and of the emitter itself [61].

In fluorescence confocal microscopy, the separation of the excitation and fluorescences light is realized by a dichroic mirror. The light passed through the pinhole is collected by a photodetector. In order to form a complete image the sample has to be scanned, hence the name scanning confocal microscope.

3.1.2. Hanbury Brown and Twiss Setup

The single-photon characteristic of a quantum emitter can be verified by the measurement of the second order correlation function, as explained in Section 2.1. Therefore,

3.1. Experimental Methods

the arrival time of all the events have to be correlated. In principle, a direct time-resolved correlation measurement is possible [62]. However, the standard technique used is a Hanbury Brown and Twiss (**HBT**) setup [63]. Such a **HBT** setup consists of two detectors instead of a single one to overcome dead time limitations. As illustrated in Figure 3.2a, incoming light is separated by a 50:50 beam splitter and guided to single-photon sensitive detectors. The second detector is armed right after the detection event of the first detector. Both of them are linked to a time correlation device which obtains the correlation between two photon events through a coincidence measurement. This means, time difference of events between the two detectors is recorded. All time-correlated events are sorted in a histogram shown in Figure 3.2b. An additional electronic delay in one path allows us also to measure negative τ . This distribution of coincidence measurements is proportional to $g^{(2)}$ in the limit of low count rates, this means τ is small compared to the average duration between two detection events.

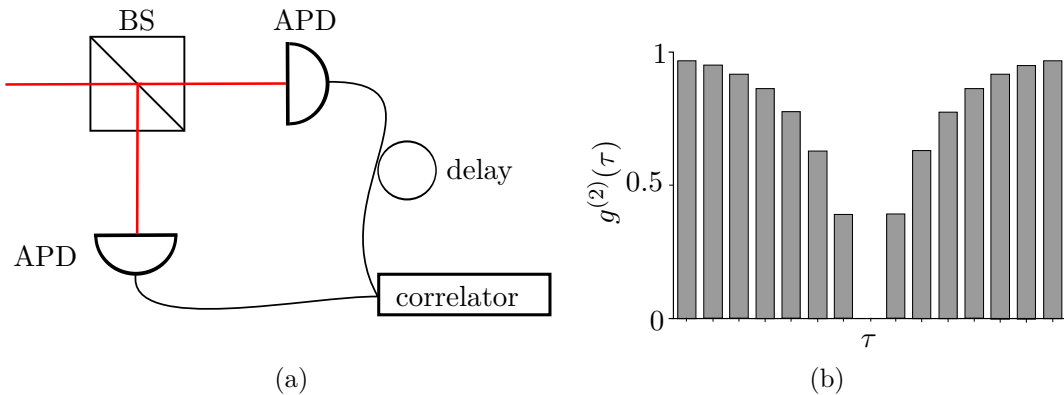


Figure 3.2.: (a) scheme of a **HBT** setup as described in the text. **APD**: avalanche photodiode, **BS**: beam splitter. (b) histogram for a single-photon emitter obtained via a **HBT** setup

3.1.3. Back Focal Plane Imaging

Back focal plane imaging (**BFPI**) is a technique to visualize the angular distribution of an emitter.

The principle of **BFPI** is Fourier optics given in standard textbooks of optics [64,65]. The scalar field at the back focal plane \hat{u} of a lens is directly related to the Fourier

3. Optical Equipment

transform (**FT**) \mathcal{F} at its front focal plane u . Given a propagation in z-direction, it follows that

$$u(x,y) \rightarrow \hat{u}(k_x, k_y) = \mathcal{F}\{u(x,y)\}. \quad (3.1)$$

This means each point (x,y) on the object plane in front of the lens is mapped into its reciprocal in momentum space (k_x, k_y) at the back focal plane. Thus, in order to obtain information about the radiation directivity of our emitter or our optical system under investigation, the back focal plane of the microscope objective is imaged (see Figure 3.3).

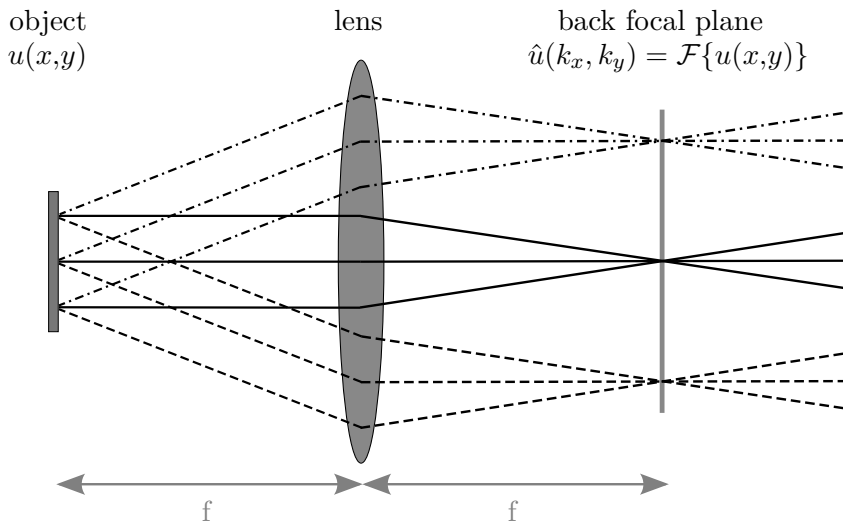


Figure 3.3.: Principle of **BFPI**. The back focal plane's image is the Fourier transform of object in front of the lens at distance of the focal length (f). Thus, the image at the back focal plane momentum space contains information about the momentum space vectors of the object.

3.2. Experimental Setup

In Figure 3.4 the scheme of the experimental setup is depicted.

Either a frequency doubled Nd:YAG continuous wave (**cw**) laser or a pulsed laser (LDH-P-FA-530, PicoQuant) with wavelengths of 532 nm excite the sample off-resonantly. Unless otherwise specified the cw laser is used. Owing to an infinity-corrected objective used the beam is collimated and expanded in order to fill out the objective's aperture. Then, the beam is reflected by a dichroic mirror, before it enters the microscope body of a Zeiss Axiovert 200. An infinity-corrected microscope

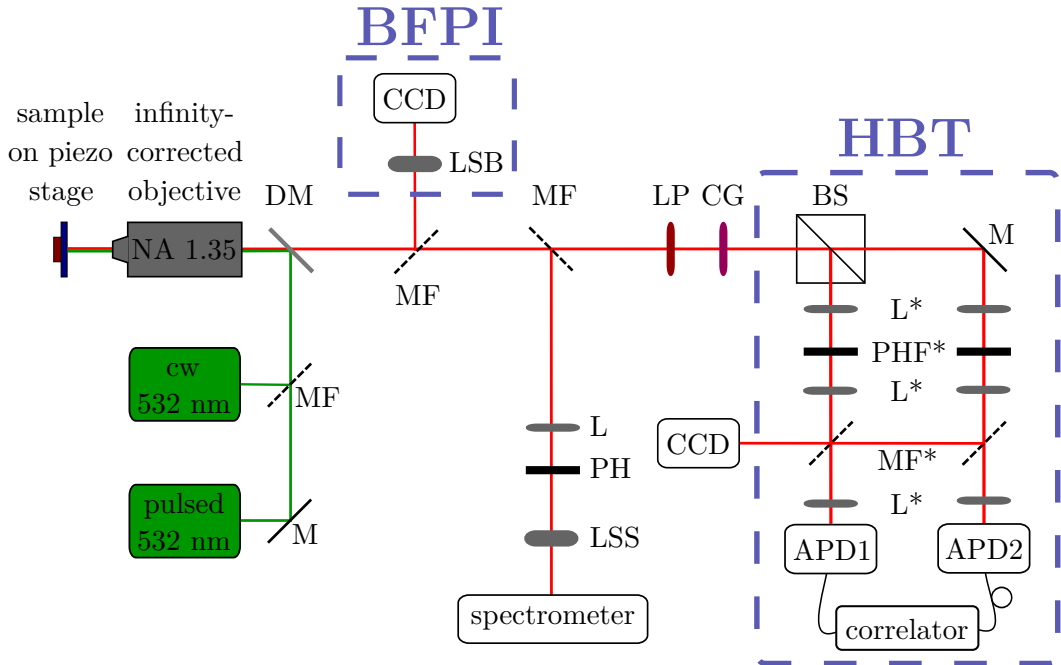


Figure 3.4.: Basic scheme of our experimental setup. **APD**: avalanche photodetector, **BS**: beam splitter, **CG**: colour glass, **DM**: dichroic mirror, **L**: lens, **LP**: longpass filter, **LSB**: lens system for BFPI, **LSS**: lens system for spectral analyse, **M**: mirror, **MF**: mirror on flip mount, **PD**: photodiode, **PH**: pinhole, **PHF**: pinhole on flip mount, **BFPI**: back focal plane imaging setup, **HBT**: Hanbury Brown and Twiss setup), the sign * indicates two objects of the same kind.

objective mounted on a 1D piezo stage (MIPOS 100, Piezosystem Jena) is applied to focus the excitation light and to collect the fluorescence. If not otherwise specified we use an oil-immersion objective Olympus UPlanSA60XO with a magnification of 60 and a numerical aperture of 1.35. The size of the focus and consequently the resolution of the confocal microscope are primarily determined by the numerical aperture and the wavelength of the light. The sample is scanned by a two-dimensional piezo stage (PXY 80 D12 SG, Piezosystem Jena). Collected fluorescence light is separated from the excitation laser by the dichroic mirror mentioned before. Then, the light can be transferred to one of the optical detection systems as a collimated beam due to the infinity corrected objective. The confocal principle is applied in the detection if needed by implementing a pinhole confocal to the focal spot in the sample. (This can be easily done. The pinhole is placed at the back focal point of a lens which focuses the collimated beam.)

3. Optical Equipment

3.2.1. Hanbury Brown and Twiss Setup

Before light from the microscope is sent to the HBT setup it is filtered by RG630 glass. A 50:50 beam splitter separates the light towards two independently adjustable pinholes. These [PHs](#) are needed for the confocal detection. Two avalanche photodiodes ([APDs](#)) (SPCM-AQR-14/SPCM-AQRH-14, Perkin Elmer) detect the light behind the pinholes with dead times of 50 ns and an quantum efficiency of 55% - 65% for light in the range of 550 nm to 800 nm [66]. The photon events are recorded in a time-correlated single-photon counting ([TCSPC](#)) via the counter module PicoHarp 300 from Picoquant with a resolution in the order of picoseconds. The time difference between the two signals originating from two detected photons is measured and binned together in a histogram. An electronic delay between one photodetector and the correlator allows to visualize also negative correlations. The counter module PicoHarp 300 offers different measurement methods. First, the time differences between each [APD](#) output is recorded in order to obtain the photon correlation, described above. Alternatively, the events at the input of the counter module can be time tagged to get the absolute arrival time of all detected photons. This recording mode provides the ability to investigate photon dynamics. Last, simply the count rate can be measured by summing up the incoming events per time.

A charge-coupled device ([CCD](#)) camera included in this setup may be used to image the different light paths after the beam splitter and check the quality of the spatial profile.

3.2.2. Back Focal Plane Imaging

The microscope objective's back focal plane is imaged onto an electron multiplier charge-coupled device ([EMCCD](#)) camera. A lens system ([LSB](#) in Fig. 3.4) consisting of conventional collecting lenses with different focal lengths is adjusted to fill out a major area of the [EMCCD](#) chip with the collected light.

3.2.3. Spectral Analysis

Fluorescence light stemming from the microscope is spatially filtered by a pinhole (confocal principle) before light enters the grating spectrograph Acton Research Corporation SpectraPro-2500i. A lens system ([LSS](#) in fig. 3.4) containing lenses and optical filters to filter the laser directs the light to the entry of the spectrometer. Using the common Czerny-Turner design the incoming light is spatially separate into

3.2. Experimental Setup

its various spectral components by the diffraction grating which are then imaged onto a [CCD](#) (Andor iDus) camera chip.

4. Measurements

The aim of this thesis is to enhance the collection efficiency of photons from single NV centres in nanodiamonds purely using an approach based on geometrical optics. The direct laser-writing (DLW) method enables the fabrication of almost arbitrary 3D architectures (Subsec. 2.4.2) which we use to tailor the emission directivity of single-photon emitters by incorporating them into special optical microstructures. In this chapter, the key experimental results obtained are presented.

In the first section, the results for the first fabricated architecture, parabolic micro-antennas, are discussed. After presenting the fabrication process we turn to pre-characterisation measurements of the NV centres chosen. Then, we concentrate on the saturation rate and angular emission of the nanodiamonds incorporated in the mirrors. Subsequently, we investigate fluorescence of different photo-resists used in DLW for an improved production process.

4.1. Parabolic Micro-Antenna

The architecture chosen to investigate their emission characteristics are parabolic mirrors as they have been used to collect light from single molecules [67, 68] and as imaging device in confocal microscopy [69–71].

In this section, a micro-scale implementation of this concept is used to enhance the light collection efficiency and to tailor the angular radiation distribution for emission into small numerical apertures. We present parabolic micro-antennas as a expedient geometry to improve light collection. When characterising the antennas, there are two important quantities to be measured – the total count rate of the saturated emitter and the angular distribution of the emission. While it is desired to have the saturated count rate as high as possible, the emission at the same time has to be as directional as possible.

First, we start with the fabrication process, followed by pre-characterisation of nanodiamonds containing NV centres. Then, we present the results obtained using our parabolic-antennas.

4. Measurements

4.1.1. Fabrication Process

The scheme of the fabricated parabolic antenna is shown in Figure 4.1. On a cover-slip, a parabolic structure is placed on a ND in its focus. A layer of silver reflects all incoming photons into the lower hemisphere. The magnesium fluoride serves as protection layer. The individual steps of the fabrication process are listed below. The fabrication steps using the techniques of DLW and EBPVD are executed by our collaboration partner, the Wegener Group, at the Karlsruhe Institute of Technology.

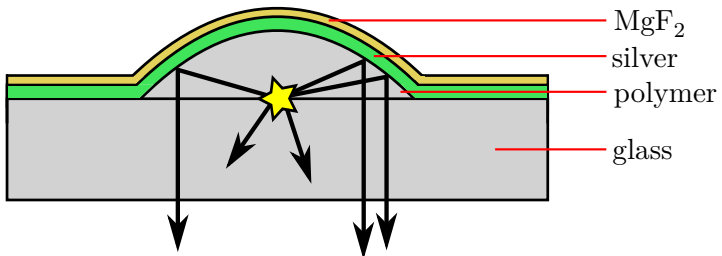


Figure 4.1.: Scheme of fabricated parabolic antenna. The NDs are spin coated onto a glass cover-slip and covered by photo-resist. A paraboloid with its focus at the NDs' location is produced via DLW. After removing the non-polymerised resist, a silver layer followed by a cover layer of magnesium fluoride for protection is evaporated.

Marker Fields

The first step is building a regular pattern which helps to locate particular NV centres. On a cover slip, a grid with fields of size $20\text{ }\mu\text{m} \times 20\text{ }\mu\text{m}$ is fabricated by DLW as shown in Figure 4.2. We will refer to them as marker fields. The grids are written using the monomer pentaerythritol triacrylate (PETA) containing O,O-diethyl chlorothiophosphate (DETC) as photo-initiator whose fluorescence gives enough contrast for the alignment in the following production steps.

In general, the DLW approach allows for pre-structuring of any substrate.

Application of Nitrogen Vacancy Centres

The nanodiamonds used for deposition on the marker grids are commercially available nanodiamonds (Microdiamant AG, MSY 0-0.05). For removal of the small NDs the water/nanodiamond solution is centrifuged. The reason to extract small NDs is that, on average, larger ones have more stable and predictable properties. Although the

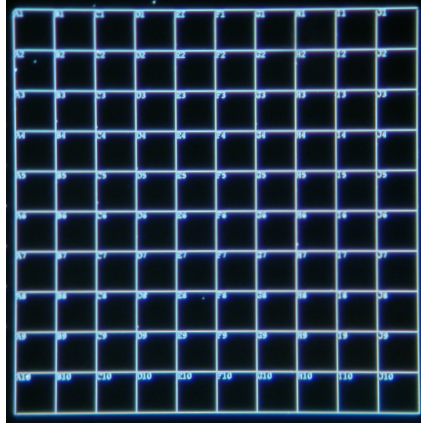


Figure 4.2.: Darkfield microscopy image of a marker grid containing $20\text{ }\mu\text{m} \times 20\text{ }\mu\text{m}$ sized fields, each indicated differently using a combination of a letter, A to J, and a number ranging from 1 to 10. (Received from the KIT)

highest count rates reported in literature [22] are achieved using blinking nanodiamonds, for the sake of reproducibility we limit ourselves to stable NV centres. A solution with a pre-determined ratio of nanodiamonds and deionised water is spin coated onto a cover slip featuring a marker field. After verifying the NV centre's single-photon characteristic its relative position on the marker field is determined. All details as well as the precision of this procedure are discussed in Subection 4.1.2. Then, the samples are processed further.

Building the Parabolic Geometry

The paraboloids which define the geometry of the mirror are produced by direct laser-writing. The photo-resist used consists of the monomer PETA and 2% of the photo-initiator Irgacure819. The photo-resist is dropcasted on the substrate and exposed building a paraboloid with its focal spot at the nanodiamond's location (see Figure 4.3a). The diameter of the paraboloid built is $10\text{ }\mu\text{m}$ with an height of $2.5\text{ }\mu\text{m}$. Then, the unexposed material is removed by development in 2-propanol and rinsed with acetone.

Reflection layer

Onto the sample, a 100 nm silver thick silver layer is evaporated as a reflection coating which is protected by an additional 30 nm thick magnesium fluoride (MgF_2) layer. A

4. Measurements

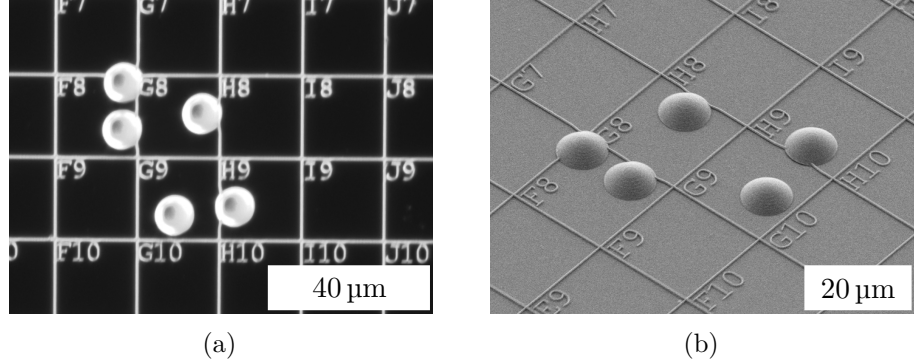


Figure 4.3.: Parabolic microstructure: (a) optical dark field image of the laser-written parabolic geometry and the marker grid after **DLW**. In an optical dark field microscopy the direct illumination beam is blocked by an aperture while diffracted beams will contribute to the image. Thus, only scattered light enters the objective, which lead to dark background with bright objects. (b) scanning electron microscope image of the paraboloids after the fabrication process is completed. A **SEM** uses a focused electron beam to form images. (Received from the **KIT**).

scanning electron microscope (**SEM**) image of the fabricated antennas is shown in Figure 4.3b.

4.1.2. Characterisation of the **NDs**

This subsection starts with investigating the precision of our alignment in the fabrication procedure. Substantially, we characterise the emission of the **NDs** on glass as well as embedded in the parabolic structure by means of determining the second order correlation function, the saturation behaviour and the angular intensity distribution.

4.1.2.1. Alignment

In order to obtain the results favoured by the parabolic mirror, the alignment of the fabrication procedure is very important. The absolute spatial values are of no special interest, but the misalignments before and after the fabrication are. Thus, only relative positions are measured.

The locations of the **NDs** are specified within a certain marker field. Using the fact that the **DLW** is a very precise method, the $20\text{ }\mu\text{m} \times 20\text{ }\mu\text{m}$ grid fields serve as an coordinate system. Each field has its own label consisting of a combination of

4.1. Parabolic Micro-Antenna

one letter and one number. We determine the locations of the NDs relative to one horizontal and one vertical border line of the grid field. The procedure of locating the relative position is simple, the sample is moved under the confocal microscope by means of the piezo-system. A rough alignment of the positions can be obtained via a confocal scan of the grid field. Then, the alignment is completed by fine-tuning the piezo to the highest count rate of the object. Here, we exploit the higher fluorescence of the NVs and the applied photo-resist compared to the substrate.

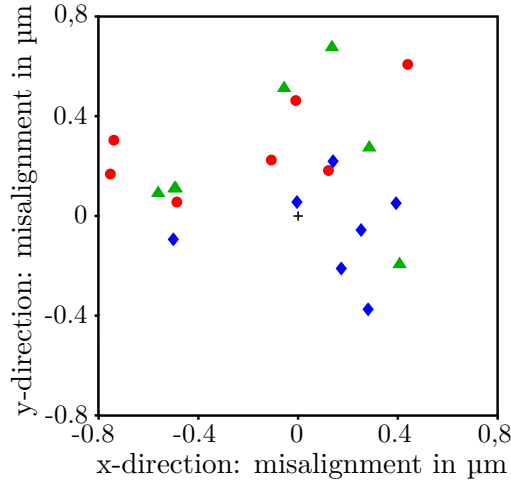


Figure 4.4.: In this figure the data sets of relative misplacements are displayed in a two-dimensional plot. The comparison of the location of the ND past the laser-writing to the ND's pre-characterised position is illustrated with the diamond sign in blue. The green triangle depicts the misalignment of the parabolic mirror's centre in respect to the location of ND prior to DLW. The red circle shows the antenna's centre compared to the ND's position after the DLW. The black plus sign displays zero misalignment.

In Figure 4.4 the alignment of three data sets are plotted:

- NVs before DLW & after the mirrors' fabrication (blue diamonds),
- NVs before DLW & the mirrors' centre (green triangle) and
- NVs after DLW and the mirrors' centre (red circles).

In general, all data sets range in the sub-micrometre region which is of importance for a reproducible fabrication process. However, the data scatter in one particular direction which indicates the locations a systematic error. The main source of error is due to the localisation procedure. The identification of the ND's position by using the

4. Measurements

brightest spot is rather subjective. This fact in combination with the pre-localisation step and the **DLW** being executed at two different laboratories, at the **KIT** and the **HUB**, enhance the possibility of misalignments. In following experiments, it has to be evaluated if a systematic misplacement occurs.

Owing to the adhesion of **NVs** onto the glass the assumption can be made that the **NDs**' position retains the same after dropcasting the photo-resist onto the glass cover slip. Thus, the comparison between the **NV** before and after the fabrication process gives information about the error introduced by the localisation process, executed by us. The averaged misplacement is evaluated to be $0.29 \pm 0.13 \mu\text{m}$. Keep in mind, that this is a combination of error occurred in the alignment. We identify the border of the marker grid and the relative position of the **NV** centre to it, which results in two localisation measurements. Since this procedure is done twice, prior and after the fabrication of the structures, the localisation steps sum up to a total of four. Thus, the individual error of the localisation itself is smaller than the alignment error determined.

The mismatch of the pre-located **NVs** and the mirror centre has an average value of $0.52 \pm 0.09 \mu\text{m}$. This enhanced value compared to the misalignment evaluated previously makes sense. As before, the localisation of the **NVs** is executed twice, plus the alignment of the parabolic mirror for the **DLW** process and the determination of the mirror's centre itself. In addition, executing the alignment at two different places is a further aggravation.

In general, the position could be measured more precisely. Using deterministic emitter switch microscopy where the spin properties of the **NV** are exploited to modify its fluorescence brightness through magnetic resonance techniques a resolution down to 12 nm is achieved [72]. Nevertheless, in the proof of principle experiment carried out here this is not necessary, since the possible improvements of the localisation seem rather small. The results obtained give reason to preserve the concept of marker grids for now. Still, an in-situ localisation of the **NVs** in the photo-resist during the **DLW** process is favoured for two main reasons, the first being an probably better alignment. The second reason is a reduced complexity of the alignment process. Measurements concerning this matter are presented in Section 4.2.

Finally, the relation between the **NVs**'location after **DLW** and the mirror centre, attracts most interest for investigating the light collecting properties of the parabolic antennas. On average, the deviation of the positions are $0.50 \pm 0.23 \mu\text{m}$. One mirror-diamond combination shows a sufficient alignment with a absolute misalignment of

4.1. Parabolic Micro-Antenna

less than $0.25\text{ }\mu\text{m}$. The data observed for its angular radiation pattern are presented in Section 4.1.4.

4.1.2.2. Second Order Correlation Function

The NDs pre-localised in the grid need to be identified as single-photon emitter. The measurement of the second order correlation is executed as explained in Section 3.2.1 with the HBT setup.

As an example, the $g^{(2)}$ function of the ND placed on the glass cover-slip at grid field F3 is depicted in Figure 4.5. The raw data are fitted using Equation 2.17 with an additional background. A non-linear curve-fitting method in least-squares sense with a 'trust-region-reflective' algorithm is applied. The black data points depict the raw data normalised to one using the background value determined in the fit. The anti-bunching, at zero time delay, is given by $g^{(2)}(0) = 0.23$ evaluated at a excitation power of $80\text{ }\mu\text{W}$. This value is an indicator that the ND contains only a single nitrogen vacancy centre. In experiments a value $g^{(2)}(\tau) < \frac{1}{2}$ marks that the observed light follows mainly an single-photon statistics. The enhanced value of the anti-bunching dip is due to additional sources, in our case most probably residual light from the resist.

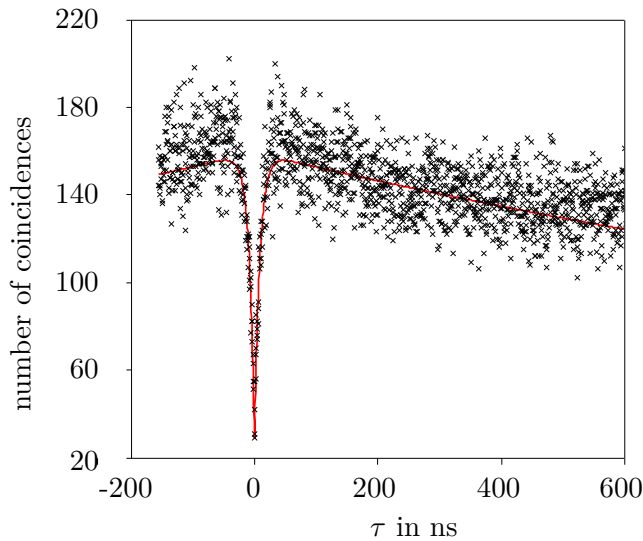


Figure 4.5.: The second order correlation measurement of the NV centre in field F3 at a excitation power of $80\text{ }\mu\text{W}$ is plotted. The data, shown as black crosses, are fitted with Equation 2.17 with an additional background value, resulting in the corresponding red curve with $g^{(2)}(0)$ being 9999.

4. Measurements

All anti-bunching values have been evaluated, showing that each emitter is source of single-photons prior the fabrication. The anti-bunching behaviour of the emitters incorporated in the structure indicate that all NDs are still single-quantum emitter. One exception is an increased value of $g^{(2)}(0) = 0.72$. Since the excitation power has not been noted no accurate statement can be made but most likely it has been an adjustment error in the confocal detection. However this nanodiamond is most likely still a single-photon emitter.

4.1.3. Saturation Intensity and Rate

The saturation intensity and saturation rate are determined by recording the NV's count rate in dependence of the laser power. Therefore, the count rates at each APPD output are summed up. Due to the outstanding count rates obtained all data shown in this section is corrected in terms of the non-linearity of the detection system (c.f. Appendix A).

Our aim is to enhance the light collection of the NV using parabolic antennas. Therefore, the saturation rate is a very important factor. However, the results of the saturation rate itself prior and after the fabrication of the parabolic mirror cannot be compared directly. The reasons are that the surroundings of the ND has been modified drastically. Instead of having an glass-air interface, the ND is now located in a homogeneous medium since the refractive indices of the glass and the photo-resist match each other approximately. Thus, the local density of states has been altered, affecting the angular emission pattern as well as the dipole's excited state lifetime [57, 73, 74]. In the case of the ND located on the glass cover-slip, this results in an asymmetric angular radiation distribution since a source preferentially emits in the medium with higher refractive index. In contrast, the source's emission is symmetrical in the homogeneous medium. The lifetime is reduced in the parabolic mirror configuration compared to the glass-air interface because of the higher refractive index which increase possible decay paths as stated in Fermi's golden rule.

Still, the rate obtained in the pre-characterisation can be used as an indicator if the number of photons collected can be enhanced in general using the parabolic configuration. This is also of interest, since high emission rates of single-photon emitters are favourable in many quantum applications.

When imaging a parabolic mirror with a diameter of $10\text{ }\mu\text{m}$ most of the light is blocked through spatial filtering. In order to collect all the photons collected by the mirror the confocal detection has to be dropped. This leads to the approach applied

4.1. Parabolic Micro-Antenna

to investigate the collection efficiency of the mirrors by evaluating the saturation rate with and without spatial filtering. Assuming an accurate alignment of the NV centre with respect to the pinhole as well as light reflected at the mirror is merely suppressed, then the count rate measured in the confocal detection stems predominantly from the nitrogen vacancy. This means, we receive an saturation rate of the NV centre embedded in the homogeneous medium. Since the mirror is at least $2.5\text{ }\mu\text{m}$ far away from the emitter, the affect of the metal on the dipole is negligible. Removing the spatial filter allows the detection of all photons blocked before. Hence, the rate obtained via the mirror can be compared with the rate determined using spatial filtering.

We evaluate the data using a modified version of Equation 2.13. Due to experimental issues as background light, e.g. of the glass substrate we introduce an additional linear background. An off-set is not needed since the data have been corrected for background, e.g. light in the room. In a non-linear curve-fitting in least-squares sense with a 'trust-region-reflective' algorithm the data are fitted with the saturation rate, the saturation intensity, and the linear background being degrees of freedom.

In general, in the case of point-like emitters, such as single NVs centres in nanodiamonds on a glass cover-slip, most of their fluorescence surpasses the spatial filtering since the pinhole size in this setup is dimensioned specifically for the NDs used. Merely background light is suppressed. This enables to receive accurate values for the saturation intensity and saturation rate using one measurement via the confocal microscope. However, special care must be taken by evaluating the saturation rate and intensity without using the confocal microscope setup. Removing the pinhole in front of the detection system results in a enormous background enhancement. The issue is that the fitting itself has three degrees of freedom, the saturation rate and intensity as well as a linear background. Usually the linear background is almost negligible . Now, with a value for the background being enormous the fit does not provide accurate results. Therefore, we use the saturation intensity which we evaluated in the measurement of the NV in the parabolic mirror via the confocal detection. We use the fact that while increasing the pump power the angular radiation pattern remains equal, and thus the fluorescence rate. This means, despite blocking most of the reflected light at the mirror surface in the confocal setup, the saturation intensity is equal without the spatial filter. Using the pre-attained values for the saturation intensity implies the reduction of the fit parameter to two. This allows the accurate fitting of the data recorded without the spatial filter.

4. Measurements

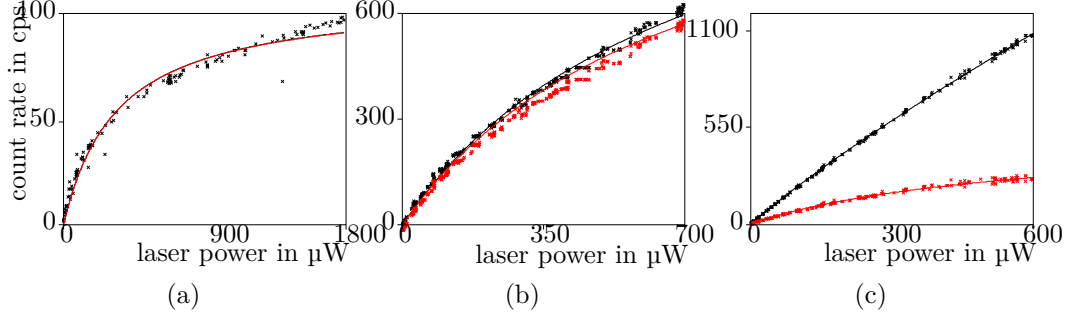


Figure 4.6.: The saturation behaviour of the nanodiamond in grid field F3 is measured. Using the confocal microscopy (a,b) the saturation intensity and in the case of NDs acting as point-like emitters also the saturation rate can be evaluated. (a) shows the saturation curve of the pre-characterisation , whereas (b,c) is measured after the mirrors are built. The saturation rate of the parabolic antenna is determined by removing the spatial filter in front of the detection in order to collect all fluorescence light stemming from the $10\text{ }\mu\text{m}$ sized structure.

In Figure 4.6 the saturation behaviour of the ND in the grid field F3 is depicted for all three configurations: ND on glass with spatial filter (Fig. 4.6a) and ND embedded in mirror with (Fig. 4.6b) and without (Fig. 4.6c) spatial filter. The data are illustrated as black dots. As described above, a modified version of Equation 2.13 with an additional linear background is used to fit the data, shown as black curve. The red data and curve depict the saturation of the NV subtracted from the linear background. The comparison between plots (a) and (b) show that the emission is altered, indeed. As explained before, the modification of the surroundings change the radiation distribution as well as the rate through an altered excited state lifetime. In Figure 4.6c the data of the NDs incorporated in the mirror is depicted recorded without the spatial filtering in the detection path. Thereto, the linear background's value determined in the fit is subtracted from the data and the fit curve, resulting in the red data points and red curve, respectively. The results of all measurements are listed in the Tables 4.1 and 4.2.

In the measurement with the ND placed on the glass substrate via the confocal microscope (Fig. 4.6a) the ND's saturation intensity and rate is evaluated to be $330\text{ }\mu\text{W}$ and $1090 \times 10^3\text{ cps}$, respectively. As mentioned above, these values serve as an indicator to determine if an enhancement of the light collection can be achieved in general. Using confocal detection the measurement of the ND incorporated in the parabolic mirror (Fig. 4.6b) we determine the saturation intensity and rate to be

4.1. Parabolic Micro-Antenna

	saturation intensity in μW	saturation rate in 10^3 cps
D9	595	1050
F3	330	1090
F9	371	845
F10	187	746
G5	103	697
G6	664	1470
average	375 ± 201	983 ± 261

Table 4.1.: The intensity and saturation value are evaluated for the NDs on the glass substrate in each grid field. The data is obtained by using Equation 2.13 with an additional linear background. The values are obtained using a confocal detection.

	saturation intensity in μW confocal	saturation rate in 10^3 cps	
		confocal	non-confocal
D9	880	1340	7180
F3	448	756	4010
F9	335	824	2470
F10	217	764	3240
G5	159	734	2850
G6	363	1020	3920
average	400 ± 234	906 ± 216	3945 ± 1546

Table 4.2.: Using Equation 2.13 with an additional linear background , the saturation rate and intensity are determined.

$448 \mu\text{W}$ and $756 \times 10^3 \text{ cps}$, respectively. The comparison of the saturation intensity of the two measurements show an enhancement by a factor of 1.4. A change is not surprising since the surrounding of the nanodiamond is modified. Instead of being located at a glass-air interface, the ND is incorporated the photo-resist, a dielectric with a similar refractive index as the glass cover-slip. Figure 4.6c shows the saturation of the NDs incorporated in the mirror recorded without the spatial filtering in the detection path. Using the saturation intensity evaluated before we can determine the saturation rate of the NV to be $4010 \times 10^3 \text{ cps}$. This means, the parabolic antenna enhance the collection efficiency of photons by a factor of 5.3 compared to the ND's value prior. In addition, this is to our knowledge the highest saturation rate obtained up to date.

4. Measurements

Since the results for only one mirror are not sufficient to make a general judgement on our approach to improve the light collection efficiency, we perform a statistical analysis of different NDs in several grid fields. We concentrate on the change in the saturation rate, since the intensity contains no information about the light collection. The results of the ND on the glass cover-slip are compared with the ones obtained after the structure is built enable us to qualify the change of the NV centre's emission properties. The averaged values (Tab. 4.2 and Tab. 4.1) show that the rate of the NV centre is reduced, which can be ascribed to the surroundings. This means the effect of the reduction in lifetime, which would enhance the rate is counteracted by the altered radiation distribution due to the homogeneous medium in which the emitter is located.

However, owing to the parabolic mirror the overall light collection is increased, supporting the geometry chosen. Moreover the light collection enhancement is outstanding. On average, the saturation without the pinhole detection is increased by more than a factor of 4. The highest achieved saturation rate for a single NV centre embedded in the parabolic mirror has a conspicuous value of 7180×10^3 cps.

We would like to qualify the accuracy of our fit model in which the background BG_{fit} was presumed to be linear. Therefore, the background BG_{exp} is determined experimentally by moving approximately $1\text{ }\mu\text{m}$ away from the ND. The data is evaluated using a linear fit, which has been accurate approximation. The results show, that the linear background for the parabolic mirrors obtained via the fit is systematically too low by around 12%. Most likely this is due to the fact, that the configuration of the linear background measurement is not completely correct. The ND at the focus is replaced with the photo-resist, wherefore the background may be enhanced which would result in a slightly higher linear background.

4.1.4. Back Focal Plane Imaging

The first goal, the increased light extraction, is achieved. The second aim is to direct the emission into a small numerical aperture which can be observed using BFPI explained in section 3.1.3. In Figure 4.7 a confocal scan of a NV centre located almost in the paraboloid's centre and its corresponding back focal plane image are depicted. The direction of the emitter's light into a very small solid angle is visible in the back focal plane image. The semi-transparent circle corresponds to the numerical aperture of the collection optics used.

In a previous approach, the NDs have been applied randomly, resulting in a parabolic antenna containing three single NVs at off-centre locations. In Figure 4.8a a confocal

4.1. Parabolic Micro-Antenna

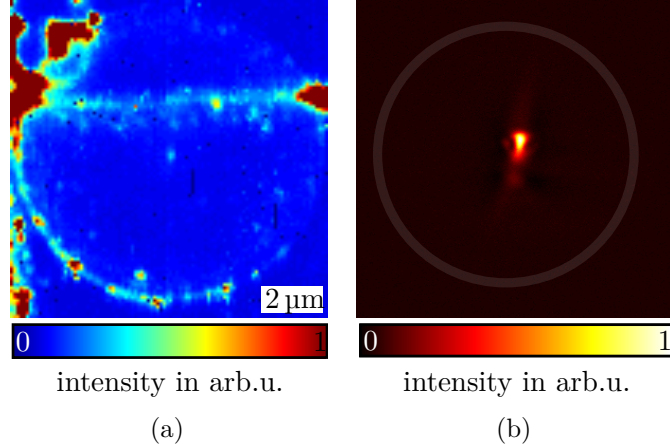


Figure 4.7.: (a):confocal and its corresponding (b) back focal plane images of a parabolic mirror with a [ND](#) in its focus.

scan is shown with the [NDs](#) marked with white dotted circles and labelled as [NV1](#), [NV2](#), and [NV3](#). Photons stemming from these emitters are reflected at the mirror under an angle with respect optical axis of the collection optics. The influence of spherical aberrations can be seen in the corresponding back focal plane images 4.8b, 4.8c, and 4.8d of the nanodiamonds [NV1](#), [NV2](#), and [NV3](#), respectively.

A possible application may be beam steering, wherefore the shape can easily be modified using [DLW](#) in order to neutralise these aberration effects.

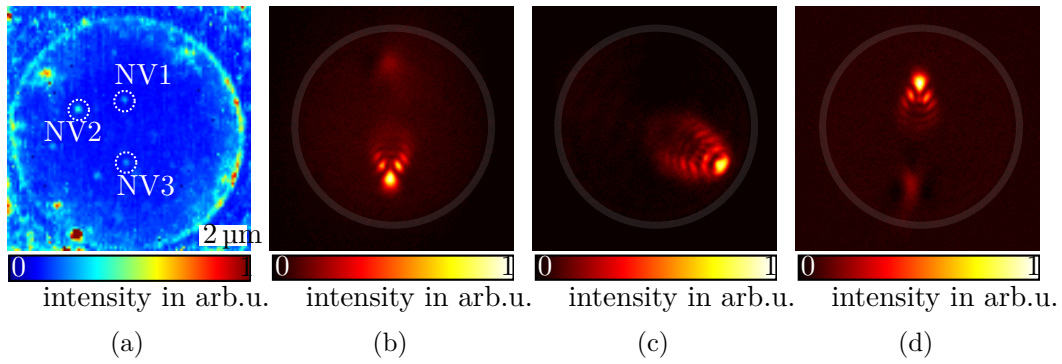


Figure 4.8.: (a):confocal scan of a parabolic mirror with randomly distributed nanodiamonds. The white dotted circles mark the off-centre positions of [NDs](#) containing one single nitrogen vacancy centre within the parabolic mirror, labelled as [NV1](#), [NV2](#), and [NV3](#). Figures (b), (c), and (d) are their corresponding back focal plane images, respectively.

4. Measurements

4.2. Photo-Resist

Because of the unexposed PI's high fluorescence it is difficult to find single NV centres during the DLW process. Here, we will investigate different PRs in order to find a suitable PR that enables the in-situ localisation of NDs during the laser-writing process. Basically all PRs consist of a photo-initiator to start the process and a monomer which is polymerised during exposure.

We measure the characteristics of three different PRs with the same monomer PETA (pentaerythritol triacrylate) but two different PI. It has to be noted that the fluorescence measurement of PR1 is not be performed. The PR's enormous fluorescence is impracticable for our aim. Thus, no further results of PR1 are presented in section 4.2.1.

- PR1: monomer PETA + 0.25% DETC
- PR2: monomer PETA + 2% Irgacure 819
- PR3: monomer PETA + 4% Irgacure 819

4.2.1. Fluorescence Measurement

In order to receive the fluorescence even for the absolute unexposed PR we block the cw laser light before starting the measurement. Once the sample is adjusted, the measurement starts. The intensity of the laser is adjusted to $0.243 \mu\text{W}$. Since the fluorescence rate is dependant on the excitation power, the laser power retains unchanged throughout all measurements.

Then, the fluorescent light of the sample is recorded in dependence of time with the absolute arrival time of the photons on the photodiodes. Thus, all the detected photons are time tagged which enables the observation of photon dynamics. In order to get information about the behaviour of the fluorescence we time bin the photons in intervals of 1 ns resulting in a histogram showing temporal behaviour of the fluorescence.

In figure 4.9, one exemplary histogram from the photo-resist PR2 (blue) and PR3 (red) are plotted. The time range before the peak exhibits the time previous to the start point of the measurement. Here the laser is blocked. The drastic increase of intensity represents the fluorescence of the entirely unexposed photo-resist – this is the count rate wanted which is about 200×10^3 cps for both PRs. However, in several measurements the initial rate varied about a factor of three for both resists wherefore

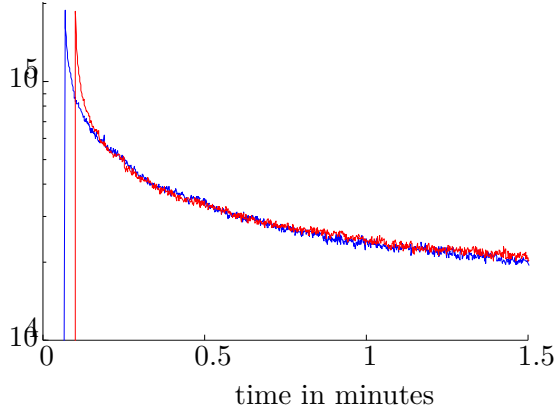


Figure 4.9.: The temporal behaviour of the fluorescence of the **PR2** (red curve) and the **PR3** (blue curve) over a time period of 1.5 minutes is shown. The lifetimes are derived from this curve by fitting an exponential function at the start and end part of the curve. Details are explained in the text.

no exact initial value for the fluorescence can be determined. Then, the photo-induced reactions starts to the point where a constant count rate is observed. After 10 minutes, the fluorescence declines to a constant value of the exposed **PR** which is determined to be 15.5×10^3 cps and 14.6×10^3 cps for **PR2** and **PR3**, respectively. We cannot conclude if the resist is fully polymerised, since the laser power used is rather low compared to a typical **DLW** values. Thus, the count rate may be even lower. However, the exposed **PRs**'s rate being ten times lower is indispensable for the ease of finding **NVs** in fabricated structures.

In general, the temporal behaviour of both curves is similar which is properly due to the use of the same photo-initiator Irgacure 819. The difference between **PR2** and **PR3** is only the **PI**'s concentration with 2% and 4%, respectively. Using the histograms the lifetime τ_{PR} of the resists can be determined in order to get quantitative properties. Figure 4.9 shows that even applying a semi-logarithmic plot the decrease is non-linear. Thus we expect two different lifetimes. Therefore in a exponential fit we evaluate the at the beginning and end of the measurement. We obtain a value of $\tau_{PR1} = 0.67$ ns and of $\tau_{PR2} = 0.64$ ns for the initial lifetime of **PR2** and **PR3** and a value of $\tau_{PR1/2} = 0.4864$ ns for both lifetimes after the exposure.

The initial aim, a **PR** allowing the pre-localisation of **ND**, needs the comparison of the obtained rates with a **ND** containing a single **NV** centre and its lifetime.

Therefore, the count rate of a **ND** on a glass cover-slip is determined to 145×10^3 cps using the same excitation laser power of $243\text{ }\mu\text{W}$ as before. The fluorescence of the unexposed resists **PRs2** and **PRs3** are around 200×10^3 cps for the histograms

4. Measurements

presented. This means, they are of the same order of magnitude as a NV centre in a nanodiamond. However, as mentioned this rate varies significant. That means that in-situ localisation of nanodiamonds by means of the fluorescence rate in the unexposed photo-resist seems not feasible with the tested photo-resists.

The Ad fluorescence lifetime of the excited state in a bulk sample is around 10 ns [16]. Assuming a similar lifetime for the nitrogen vacancy centre in nanodiamonds this exhibits a lifetime 20 times longer than the results of the resists. This means, a time-gating measurement seems to be capable of resolving the nanodiamond's fluorescences in the resist despite its high rate. In addition, a better spatial filtering, purely adjusted to find point-like nitrogen vacancy centres could enhance the signal to noise ratio so that the detection of NV centres during exposure can be achieved. However, this seems not feasible.

4.2.2. Spectra

Beside the approach to locate nanodiamonds in the unexposed photo-resist, the finding of them in the exposed PR is indispensable. Even a high PR's fluorescence is not that fatal if its spectrum does not (or only weakly) overlap with the NV centres' fluorescence spectrum. The recorded spectra of the three PRs are shown in figure 4.10. We do not use any spectral filtering. The laser light, at 532 nm, is not depicted.

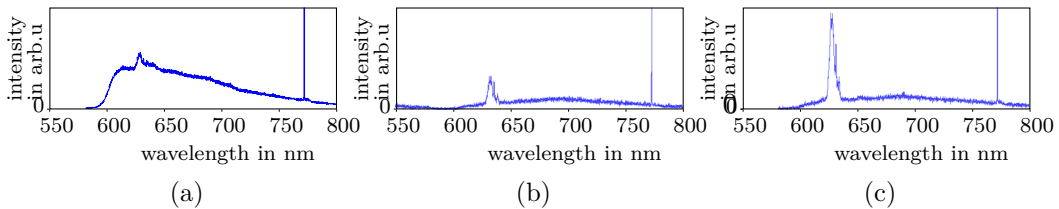


Figure 4.10.: Spectra of the sample (a) PR1 ,(b) PR2, (c) PR3

The peak at 775 nm is not a feature of any particular photo-initiator since it is observed in all three cases. The origin is not known.

In all three cases, the intensity profile is in the spectral range from 625 nm to 640 nm. However, the features show that the PR's fluorescence is dependant on the type of photo-initiator used. Compared to the common fluorescence spectra of the PI the spectra of all PIs is strongly red-shifted which probably stems from the incorporation in the monomer during the polymerisation.

4.2. Photo-Resist

By comparison, as shown in Figure 2.2b and explained in section 2.2.3 the NV's fluorescence range from 637 nm [46] to 800 nm. That means, the wavelength of the spectra is not perfectly separable from the nitrogen vacancy one, but still, a fraction of the PR's fluorescence can be filtered.

The spectra b) and (c) may allow to compare the photo-initiators concentration. Since the laser power at which the spectra have been taken is not reproducible any more, we compare their signal to noise ratio. This is not an accurate evaluation, but it seems that the signal to noise relation is doubled in the PR3's spectra. Furthermore, using the results from above that the temporal decrease of both PRs exhibit similar behaviour as well as the similar fluorescence rates after the exposure, one might assume that the fluorescence of the exposed photo-resist is dependent of the PI's concentration in the PR. This is not a statement, but it can be considered in following experiments.

In conclusion, the search for an PR needs to be continued to avoid the alignment procedure in the fabrication process (sec. 4.1.1). But the results are promising, since it seems that the detection could be possible using additional Furthermore, the resist's spectrum has to be considered in the development as a possibility to filter its light. First, for the ease of finding the NV and second to reduce background light in measurements. The members of the Wegener Group keep on working to achieve a progress soon.

5. Modified Solid Immersion Lenses – Finite-Difference Time-Domain Calculations

The content of this chapter will be published in a paper.

Finite-difference time-domain ([FDTD](#)) is a technique to numerically solve problems in computational electrodynamics. The analysis is conducted using a commercial [FDTD](#) simulation software (Lumerical, FDTD Solutions 7.5).

In section [4.1](#) it has been shown, that the technique of two-photon direct laser-writing enables the fabrication of $10\text{ }\mu\text{m}$ sized parabolic antennas, moreover nearly arbitrary three-dimensional microstructures can be manufactured in high quality [[24](#), [75](#)]. This means, almost any architecture can be taken into consideration to enhance the light collection and emission directivity of a point-like emitter. Here, we show simulations for designs based on the geometry of solid immersion lenses ([SILs](#)) – lenses which have a hemispherical form. We will modify their shape by using elliptical instead of spherical cross-sections.

In this chapter a short introduction of the basic concept of the [FDTD](#) method is given. After preliminary remarks about the idea of employing non-spherical shaped [SILs](#), referred to as modified [SILs](#) ([mSILs](#)), we present the theoretical guidelines for the novel design concept. Then, using the [FDTD](#) implementation, we illustrate the advantageous light collection properties of [mSILs](#) followed by their mode profile characteristics.

5.1. The Finite-Domain Time-Differential Method

The finite-domain time-differential ([FDTD](#)) method is a technique to numerically analyse electrodynamics using the differential Maxwell's equations within a certain computational domain. The idea is to solve the differential equations at certain points on a space grid and evolving the electric and magnetic field forward in time.

5. Modified Solid Immersion Lenses – Finite-Difference Time-Domain Calculations

In classical electrodynamics the Maxwell equations describe the electromagnetic field in a medium as a system of inhomogeneous partial differential equations of first order by means of electric field strength \mathbf{E} , the electric displacement $\mathbf{D} = \mathbf{D}(\mathbf{E})$, the magnetic field strength \mathbf{H} , and the magnetic flux density $\mathbf{B} = \mathbf{B}(\mathbf{H})$, which are all functions of space and time (\mathbf{r}, t) . In the following, we will group \mathbf{D} together with \mathbf{E} and \mathbf{B} together with \mathbf{H} using the terms electric and magnetic field, respectively. Using the SI-units version [76], the Maxwell equations take the form:

$$\nabla \times \mathbf{H} = \mathbf{J} \frac{\partial \mathbf{D}}{\partial t} \quad (\text{Ampere's law}), \quad (5.1)$$

$$\nabla \times \mathbf{E} = - \frac{\partial \mathbf{B}}{\partial t} \quad (\text{Faraday's law}), \quad (5.2)$$

$$\nabla \cdot \mathbf{D} = \rho \quad (\text{Gauss' law}), \quad (5.3)$$

$$\nabla \cdot \mathbf{B} = 0 \quad (\text{Gauss' law for magnetism}), \quad (5.4)$$

where $\rho(t, r)$ is a given volume density of electric charge in the medium and the vector \mathbf{J} stands for the volume density of electric current.

The fundamental FDTD algorithm was first proposed by Kane Yee in 1966 [77]. Basically the algorithm can be summarised as follows:

The physical domain as well as the differential equations are discretised. As a consequence, the simulation region is structured in discrete mesh cells with the electric and magnetic field components staggered in both space and time. Furthermore, the derivatives in equations 5.2 and 5.3 are replaced with finite differences. The magnetic and electric field are evaluated subsequent to each other at every mesh cell. This can be derived from equation 5.2 where the change in the electric field in time, $\frac{\partial \mathbf{D}}{\partial t}$, is dependent on the change in the \mathbf{H} field across space, $\nabla \times \mathbf{H}$. This 'time-stepping' relation points out, that, at any point in space, the unknown value of the electric field in time depends both on the stored value of the electric field and on the numerical solution of the curl of the local magnetic field in space. In reverse, the magnetic field at any point in space depends on the stored value of the magnetic field as well as on the curl of the electric field (c.f. eq. 5.3). Solving the differential equations yields the updated electric and magnetic field at the corresponding space-time points. These iterations are repeated with the 'shifted' fields until the desired duration of the simulation is reached.

The FDTD method provides a solution for the electromagnetic fields in some finite regions of space, i.e. the computational simulation domain. However, in our

case we are not interested in the fields at the region we have modelled (near-field), but rather on the fields far away (far-field). The commercial **FDTD** software used, Lumerical **FDTD** solution 7.5, has a algorithm implemented for a near-field to far-field transformation based on an algorithm given in [78]. We refer to this book for details. In essence, it states that knowing the electromagnetic field components on the surface of a closed box within the simulation region, this near-field can be projected to any point outside the box.

5.2. Modified Solid Immersion Lenses

5.2.1. Concept

In basic confocal microscopy the numerical aperture (**NA**) is limited to 1, since only light emitted in one hemisphere can be collected. However, total internal reflection (**TIR**) further reduces the **NA**, as explained in section 2.2.4. A way to increase the light collection is the use of solid immersion lenses which are truncated spheres made of a transparent medium with an high refractive index n . **SILs** relax the constraints imposed by **TIR** at the interface of materials with different refractive indices [79, 80]. Hence, total internal reflection is inhibited at the medium-**SIL** interface.

However, attention must be paid for **TIR** at the lenses interface to air. To extract light originating from the lens two common **SIL** geometries are used. First, the standard **SIL** is a sphere cut in half. Placing an emitter in the **SIL**'s centre on the flat site mitigates total internal reflection at the lens-air interface. All light hits the surface perpendicularly. In an approach where a nanodiamond containing a single **NV** centre has been located at the centre of a **SIL** made of ZrO_2 it has been shown that most of the light from the emitter is directed to very shallow angles [22]. Thus, the collection optics are still restricted to large numerical aperture for an accurate light collection. The second geometry used is called Weierstrass or super-hemisphere **SIL** exhibiting a truncated sphere with a special height h . The height is given by $h = (1 + \frac{1}{n})R$, where R is the sphere's radius and n the refractive index of the lens. This type of lens represents a non-linear image system with substantial aberration [23]. However, in the case of extracting single-photon emission, this is irrelevant. Light originating from the flat surface's centre of the lens is refracted into slightly smaller angles [80] compared to the standard **SIL**. This reduction of the angular light emission is required in order to use collection optics with lower numerical apertures. Especially in cases where it is difficult to use large numerical

5. Modified Solid Immersion Lenses – Finite-Difference Time-Domain Calculations

aperture optics, e.g. when extracting light from samples in a cryostat, this property is advantageous.

Heretofore, the lenses are used just to prevent light losses due to total internal reflection at the medium-air interface. Our idea is to take advantage of **TIR**. Via total internal reflection, we want to modify the light's propagation direction. By optimising the structures curvature light emitted in large angles can be directed into smaller ones, resulting in a reduced numerical aperture. Thus, not only the light collection is enhanced but additionally the mode-profile can be tailored. Still, the overall amount of photons emitted in one half sphere cannot be increased since it is determined by the difference in the refractive indices of **SIL** and surrounding medium.

5.2.2. Geometry

The difference between **SILs** and modified **SILs** is the expansion to spheroidal geometries. Details about the geometry of modified solid immersion lenses (**mSILs**) are depicted in Figure 5.1a. The minor and major semi-axis of the spheroid are marked as a and b , respectively. The height of the spheroid is given by h . Rotating along b , the three-dimensional spheroid is obtained.

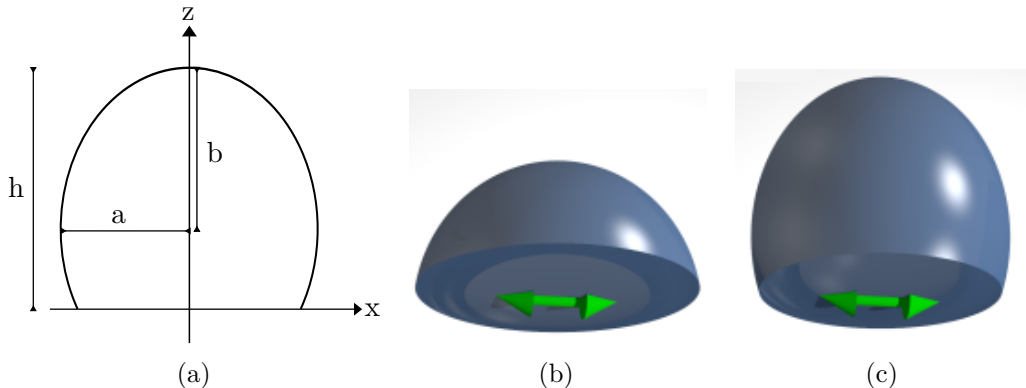


Figure 5.1.: Illustration of the **mSIL**'s spheroidal geometry 5.1a. The parameter r is the ratio between the short and long axis a and b , respectively. The degree of truncation s is the height of the spheroid along the optical axis in terms of height of a spheroid, which is two times the semi axis b . 5.1b and 5.1c show illustrations of a standard **SIL** with parameter $r = 1$ and $s = 0.5$ and one specific **mSIL** with parameter $r = 0.8$ and $s = 0.75$, respectively

5.3. Simulation Settings

In general, the equation of a spheroid with a symmetry along the z-axis (or semi-axis b) is given by:

$$\frac{x^2 + y^2}{a^2} + \frac{z^2}{b^2} = 1. \quad (5.5)$$

For ease, the dimensionless parameter r is defined as the ratio of a to b :

$$r = \frac{a}{b} \quad (5.6)$$

As an indicator of the degree of truncation, we introduce the parameter s defined as the fraction of the height h along the optical axis of the truncated spheroid to the height of the entire spheroid:

$$s = \frac{h}{2b}$$

The maximal value for s is 1 since the height h of the spheroid is limited to $2b$.

The **mSILs**' geometry is altered varying two parameters: the ratio r between the spheroid's semi-axes which changes the surface curvature, and the degree of truncation s . Its modification results in a change of the angle of incidence at the lens-air interface.

The ratio r is varied from 0.1 to 1 in increments of 0.1. Since the major axis of the spheroid is set to a constant value of $b = 5 \mu\text{m}$, a change in r implicates a change of a from $0.5 \mu\text{m}$ to $5 \mu\text{m}$. The second parameter, the truncation s , is changed in steps of $0.416 \mu\text{m}$, which is equal to $\frac{b}{12}$. Hence, the size of the different **mSIL** configuration varies around $1 \mu\text{m}$ to $10 \mu\text{m}$.

In Figure 5.1b a standard **SIL** with parameter $r = 1$ and $s = 0.5$ is depicted. The illustration 5.1c shows one specific **mSIL** with parameters $r = 0.8$ and $s = 0.75$, as an example.

5.3. Simulation Settings

Each **mSIL** simulation is performed using an equal sized calculation domain in order to receive comparable results. The grid resolution is obtained calculating the emission characteristic of the same lens configuration, but varying the grid size. The mesh resolution at which the calculation results converge is chosen. The grid's largest mesh cell has a size smaller than 30 nm . The number of mesh points per wave length is at least around 24, as the quantum emitter was approximated by a dipole emitting at a central wavelength of 717 nm . In Figure 5.1b and 5.1c the dipole is indicated

5. Modified Solid Immersion Lenses – Finite-Difference Time-Domain Calculations

by a green arrow, placed at the flat surface of the truncated spheroid. Due to the rotational symmetry of the [mSIL](#) geometry, only two orthogonal orientations need to be evaluated in order to calculate the optical properties of every other dipole orientation simply by the superposition of these two.

It must be possible for light to exit the simulation domain without interfering with the fields inside of the domain. This can be done by choosing appropriate boundary conditions. In our simulations, the computational domain is surrounded by an artificial absorbing layer, the so called perfectly matched layer ([PML](#)). [PMLs](#) are not only designed to absorb light totally but additionally to prevent its reflection back into the computational area. Computational time and resources can be saved exploiting symmetric and anti-symmetric boundary conditions. Owing to the spheroid's rotational symmetry both symmetric and anti-symmetric boundaries along the x- and y-axes can be chosen. However, due to the dipoles orientation, the boundaries have to be adjusted dependant on the dipole implemented. For the dipole oscillating along the z-axis, both boundaries are set symmetrically. On contrast, the dipole oscillating parallel to the bottom of the lens has an anti-symmetric symmetry along this specific axis, whereas the other boundary retains symmetric.

The [mSIL](#) is placed in a simulation region surrounded by air with an index of $n_{air} = 1$. The [mSIL](#)'s material is approximated applying an index of refraction of $n_{mSIL} = 1.5$ without dispersion to match the properties of glass and commonly used photo-resists.

In order to quantify the tailoring effect of the [mSILs](#), the far-field emission pattern is calculated. Therefore, knowledge is needed about the electric and magnetic field at a surface of a closed box surrounding the lenses. To achieve comparable results in all calculations, an equal box size is chosen for each simulation.

We would like to mention that we focus on a purely geometrical approach. Hence, only results obtained from [mSILs](#) simulations where the total energy in the computational volume is declined to 0.01% of the initial energy injected within a time of 600 fs are used. Results from simulations, which do not meet this condition, are excluded. These resonance effects occur due to total internal reflection in some lens configurations where the light emitted into the lens cannot escape.

5.4. Results of the FDTD Simulations

5.4.1. Radiated dipole power

In every calculation the dipole power is set to have the same value. However, it has to be considered that the dipole's emission is modified in the presence of a planar surface. A dipole located at an interface preferentially radiates in the material with higher refractive index. Changing the **mSIL**'s geometric parameters results in different sized air-medium interfaces at the **mSIL**'s bottom. Hence, for the variety of simulated geometric configurations the total power emitted by the dipole [81] as well as its angular radiation pattern changes [57, 73]. This means, not only the dipole's total power emitted has to be evaluated for each **mSIL** simulation, but furthermore the data obtained for the far-field radiation pattern, needs to be normalised in order to compare the results of different **FDTD** simulations.

There are mainly two options: to normalise with respect to the power emitted into the upper hemisphere or to the total emitted power. The first is necessary in order to compare the light compressing characteristics of each lens configuration, whereas the second is considered for evaluating the overall light collection efficiency as well as the coupling efficiency to an optical fibre.

5.4.2. Light Collection Properties

In order to evaluate the property of a **mSIL** to collect light its angular emission distribution is needed. Therefore, the far-field emission pattern of each **mSIL** configuration is calculated using the simulation settings described in section 5.3. As mentioned above, the light collection can be evaluated using two different normalisations. Since we are interested in the compressing effect, the normalisation to the power emitted in the upper hemisphere is chosen for all data presented in this section.

In Figure 5.2 far-field distributions for a standard and modified **SILs** are shown, exemplary. Compared to a standard solid immersion lens geometry the **mSILs**' angular light distributions are compressed into small solid angles for both dipole orientations. In order to quantify this observation, the far-field distribution is integrated discretely over a certain **NA**. Hence, the normalised angular emission distribution can be presented as a function of the numerical aperture. This means, we can compare the compressing effect of the distinct modified solid immersion lenses.

As an example, light collection in dependence of the numerical aperture for two geometries are compared, one specific **mSIL** with parameters $r = 0.8$ and $s = 0.875$ a standard **SIL**, depicted in Figure 5.3. For both dipole orientation parallel (Fig. 5.3a)

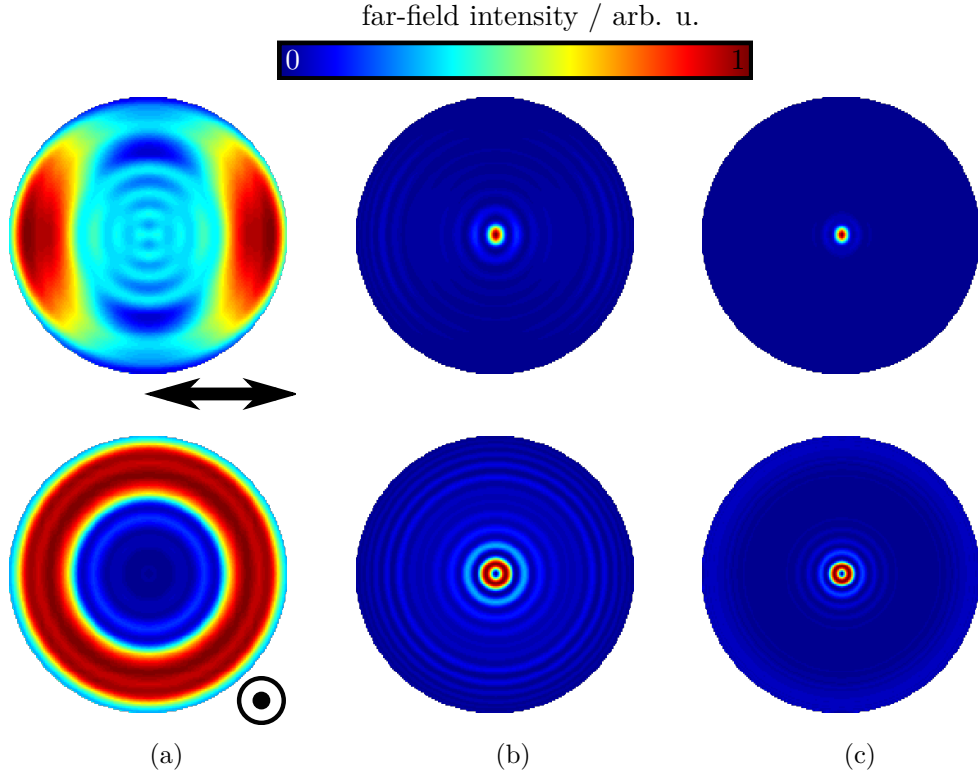


Figure 5.2.: The angular far-field intensity distributions for a dipole parallel to the lenses' planar surface are depicted in the top line while the dipole orientated perpendicular to the surface is shown at the bottom row. (a) are the distributions for a standard **SIL**, whereas (b) and (c) are the far-fields for **mSILs** with parameters $r=0.8$, $s=0.875$, and $r=0.6$, $s=0.708$, respectively. The colour scale shows the light intensity normalised to the total intensity radiated in the upper hemisphere

as well as perpendicular (Fig. 5.3b) to the planar surface of the lenses the directivity can be increased drastically using the **mSIL** design. Indeed, with a numerical aperture of 0.2 the simulation indicates that the collected intensity is about 276 times higher compared to a standard hemispherical **mSIL**. Still, the amount of light collected with this exemplary **mSIL** for a **NA** as low as 0.2 is 27.2 %.

Distinct optical systems require different light collection and compressing properties of the lenses. Therefore, dependent on the characteristics to match, different **mSIL** geometries can be preferential. In Figure 5.4, the combination of values of the best suited **mSILs** for a given numerical aperture is plotted as black dotted line. The red and green line are the collection efficiencies of standard and Weierstrass

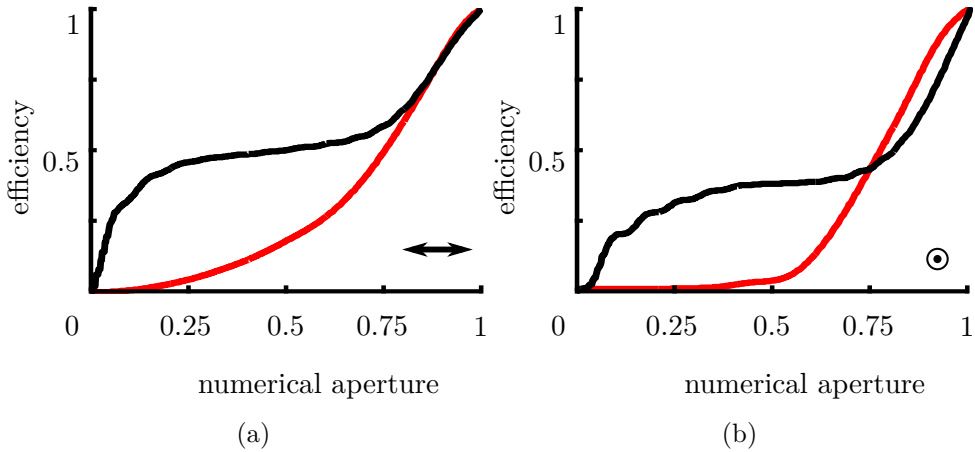


Figure 5.3.: Collection efficiency of a **mSIL** with parameters $r = 0.8$ and $s = 0.875$ (black line) in comparison with a standard **SIL** (red) for a dipole orientation (a) parallel and (b) perpendicular to the **mSIL**'s interface. Especially for small numerical apertures of the collection optics the photon collection gets enhanced. All efficiencies are normalised to the intensity emitted into the upper hemisphere.

SIL configuration, respectively, which serve as comparison. Especially at lower numerical apertures the **mSILs** surpass the light collection efficiencies of standard and Weierstrass **SIL** geometries by far for both dipole orientations. On top of that, for a **NA** as low as 0.3 more than 90 % of the light in the upper hemisphere can be collected.

Exploiting total internal refraction in combination with the refraction properties of **mSIL** geometries, the propagation direction of a dipole emitter can be altered to match the optical system's numerical aperture. Hence, the light collection efficiency can be increased drastically. Still, these structures cannot increase the overall amount of photons emitted in one half space. This is given by the difference in the refractive indices of **SIL** and the medium surrounding the emitter.

5.4.3. Mode profile

Besides collecting omnidirectional emitted light, the main issue in utilising light from a single-photon emitter is its transfer to different locations. Commonly optical fibres are used for transmission over longer distances. Single mode fibre exhibits a Gaussian shaped intensity profile. Hence, we exploit the **mSIL**'s ability to shape the mode profile of the emission distribution in addition to redirect light in small numerical

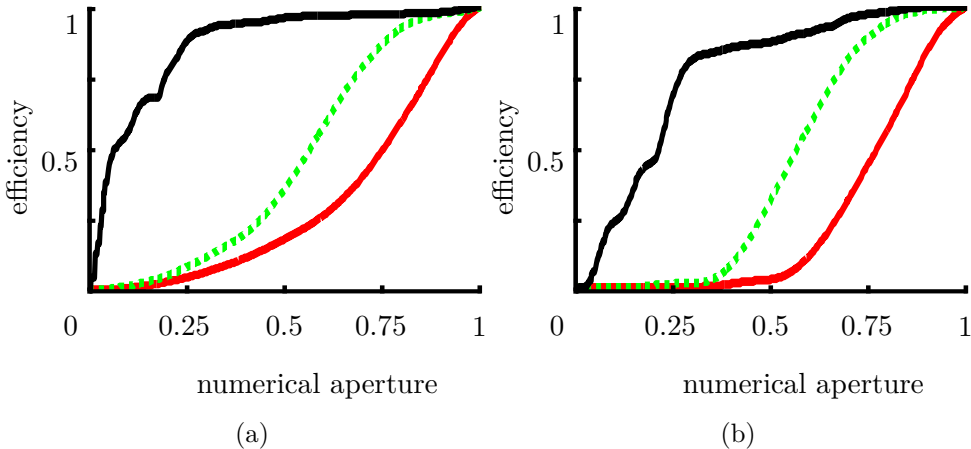


Figure 5.4.: Collection efficiency of the best mSILs (black line) compared with standard (red) and Weierstrass SIL (green). Using the best suited mSIL for a given numerical aperture results in a tremendous enhancement of light collection. The plots in a) and b) are dipoles parallel and perpendicular to the interface, respectively. All efficiencies are normalised to the normalized to intensity emitted into the upper hemisphere

aperture. We calculate the overlap between the intensity profile of a Gaussian beam with an amplitude of one and the far-field distribution which is normalised to the total power emitted by the dipole. Thus, we obtain the fibre coupling efficiency θ of the dipole-lens configuration.

The results of the overlap calculations are shown in Figure 5.5. For every NA the result of coupling efficiency θ of the best suited mSIL is shown. The graphs indicate that light originating from a single dipole emitter can be coupled efficiently to an optical fibre with the help of mSILs. For example, a mSIL with parameters $r=0.4$ and $s=0.87$ will collect over 65% of the emitted power into a Gaussian beam while only needing a NA of 0.32.

In conclusion the simulation results of the novel design concept of modified solid immersion lenses indicate that lenses can effectively increase the radiation intensity at small NAs while shaping the mode-profile of the emission. These features enable efficient interfacing of optical emitters, such as nitrogen vacancy centres without the need of additional optical elements. A drastic decrease in the solid angle of emission compared to the SILs has been shown, which enables high photon collection efficiency even with low numerical aperture optics. Furthermore, the remarkable intensity overlap of the radiation distribution with a Gaussian beam enables easy fibre coupling and transmission of the light.

5.4. Results of the FDTD Simulations

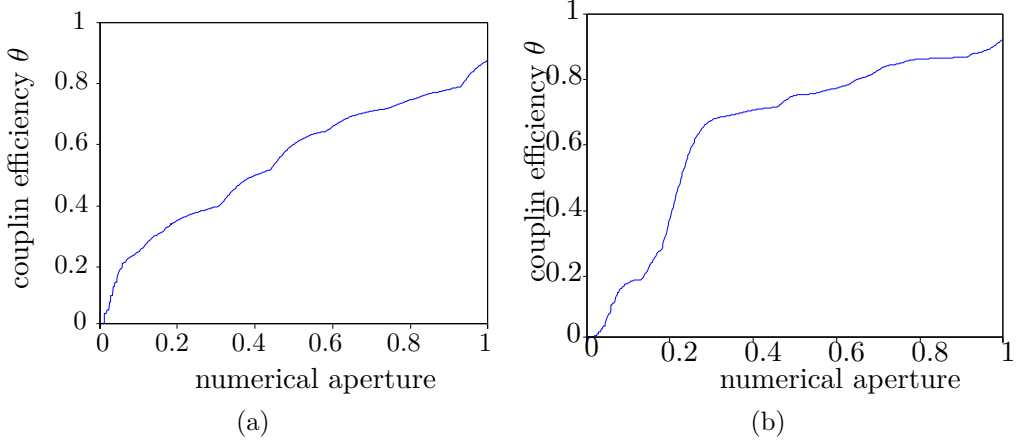


Figure 5.5.: The coupling efficiency θ between a Gaussian shaped mode and the far-field of the best suited **mSILs** for a certain numerical aperture for a dipole orientation (a) perpendicular and (b) parallel to the planar surface of the lens.

Direct laser-writing offers the possibility to build these structures on a sub-micron scale, shown in Figure 5.6. The truncation parameter is set to $s = 0.5$ and the semi-axes a and b are altered in increments of $2 \mu\text{m}$ from $2 \mu\text{m}$ to $14 \mu\text{m}$. The pedestal is added to the **mSIL**'s bottom to simulate the air-lens interface. In this attempt, no emitters are incorporated in the structures.

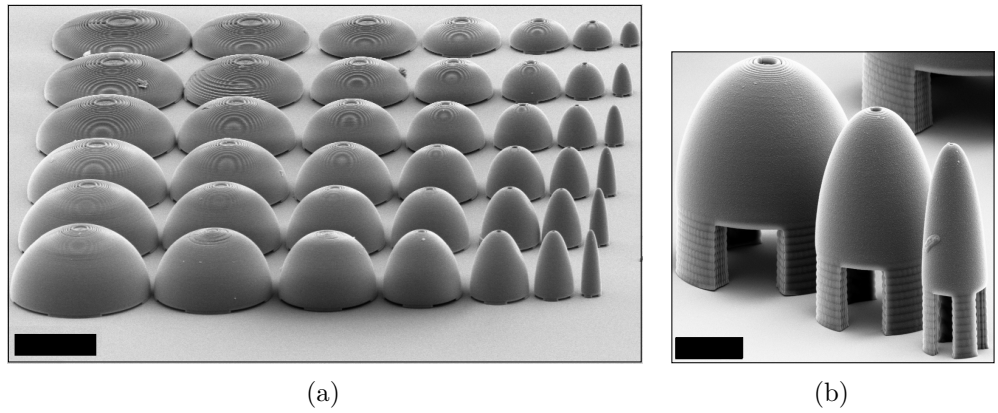


Figure 5.6.: Modified solid immersion lenses fabricated via [DLW](#) without the incorporation of nitrogen vacancy centres in the photo-resist. The pedestal is built in order to receive an air-medium interface at the lenses' bottom. The truncation parameter is set to $s = 0.5$. (a) the semi-axes a and b are varied from $2\text{ }\mu\text{m}$ in steps of $2\text{ }\mu\text{m}$ to $14\text{ }\mu\text{m}$ showing the high accuracy of the [DLW](#) technique. The scalebar is $10\text{ }\mu\text{m}$. (a) shows the smallest mSILs built with $b = 2\text{ }\mu\text{m}$ and from left to right $a = 2\text{ }\mu\text{m}$, $4\text{ }\mu\text{m}$, and $6\text{ }\mu\text{m}$, respectively.

6. Conclusion

The aim of this master thesis is the enhanced light extraction of nanodiamonds containing single nitrogen vacancy centres embedded in three-dimensional laser-written structures. By exploiting a 'simple' geometrical approach, the omni-directional emission of the point-like emitter can be countered. This means, light refraction and constraints imposed by total internal reflection are sufficient to redirect the photons emitted from the NV centre in a favoured way. We have pursued two approaches the first being the experimental investigation of ND embedded in parabolic antennas as well as a the computational evaluation of a novel design concept based on truncated spheroids.

Focusing on the parabolic mirrors, we have shown the drastic increase of the photon collection efficiency as well as the emission directivity of single NV centres embedded in the mirror's focus. The fabrication procedure in an aligned way has been demonstrated to be accurate by means of locating nanodiamonds prior the direct laser-writing in the proof of principle experiment carried out here. On average, the saturation of the nanodiamond embedded in the mirror can be increased by a factor of 4 with count rates of up to 7180 counts per second from a single nitrogen vacancy centre – without correcting for losses in the optics and detector efficiencies. In addition, single NVs at off-centre locations within the parabolic geometry are capable of beam steering capability on condition that a modified parabolic shape in order to eliminate aberration effects. Using DLW this can easily been implemented in future works.

An in-situ localisation of the nitrogen vacancy centre during the DLW process is favourable for a facilitated alignment procedure. Hence, a photo-resist is quested which fluorescence varies from the nitrogen vacancy centres in terms of the absolute emission rate, the fluorescence lifetime and the spectral range. The results of the monomer DETC mixed with the photo-initiator Irgacure 819 indicate, that the in-situ laser-writing can be achieved. However, the use of this specific photo-resist for such an approach is rather questionable due to its high fluorescence when unexposed and its spectrum being in same range as NVs. Still, its lifetime being around 20 shorter

6. Conclusion

than the NV centre's in bulk diamond [16], allows for an efficient time-gating which might enable the ND's detection much easier. The search for a suitable resist is still in progress , and the it seems that a progress can be achieved soon. The development of a the photo-resist is done by the members of the Wegener Group at the KIT.

The potential of the geometrical approach is not only limited to increase light collection but also to tailor the light's mode profile. In finite-domain time-differential calculations a novel design concept, the so called modified solid immersion lenses, have been proofed to drastically increase the light collection by compressing the propagation direction of a dipole emitter in small numerical apertures. Furthermore, the intensity overlap between the Gaussian beam, to match the profile of a single-fibre mode, and the mSILs' radiation distributions shows an remarkable overlap which enables easy fibre coupling and transmission of the light.

In general, the potential of our approach is tremendous, since the method of direct laser-writing enables the fabrication of almost limitless geometrical sub-micrometre sized architectures to redirect light in a desired way. A more sophisticated ansatz is to design an optical system that produces a prescribed light distribution for a given source. There are several methods of one being the Simultaneous Multiple Surfaces method applications which require light concentration [82].

A. Non-Linearity Correction

Throughout this thesis, we work with high intensities which are unusual in the field of single-photon counting. Due to these high count rates, the non-linearity of the APDs and the electronics cannot be neglected – a calibration curve for the count rate is needed.

A common problem encountered in detection systems recording discrete events, are dead time limitations. After each event the system is not immediately able to record another event. This time duration in which the system is disabled/blocked is called dead time. An event happening during the system's dead time is simply lost. With an increasing event rate, the detector will reach a saturation equal to the inverse of the dead time. This is the non-linear behaviour of the instrument observed in the experiment. As a consequence, dead time corrections need to be applied.

The rate R_{out} measured with the detection system is related to the rate R_{in} impinging on the APDs via

$$R_{in} = R_{out} \cdot c_D, \quad (\text{A.1})$$

with the dead time correction factor c_D [83, 84]. This factor depends on the dead time τ_D of the detection system and the actual count rate. It can be approximated as follows:

$$c_D = \frac{1}{1 - \tau_D R_{out}}. \quad (\text{A.2})$$

This approximation is accurate as long as in the condition

$$\frac{R_{out} T}{R_{in} \tau_D} \gg 1 \quad (\text{A.3})$$

is complied for a measurement interval T [84].

A quantitative description of the non-linear behaviour requires a light source of an known power shining onto the detection system, in our case APDs in combination with the electronics. Therefore, the laser normally used to excite the sample is utilised. The dependence of the APDs' count rate on the laser power is recorded. The photodiode measuring the laser power is not linear at low laser powers. Therefore,

A. Non-Linearity Correction

different neutral filters are applied to attenuate the laser, wherefore we can achieve accurate results of the linear and non-linear regions of count rates. In Figure A.1a the obtained data is plotted. The colours show measurements with different neutral filters. As expected, a decrease at high count rates can be observed.

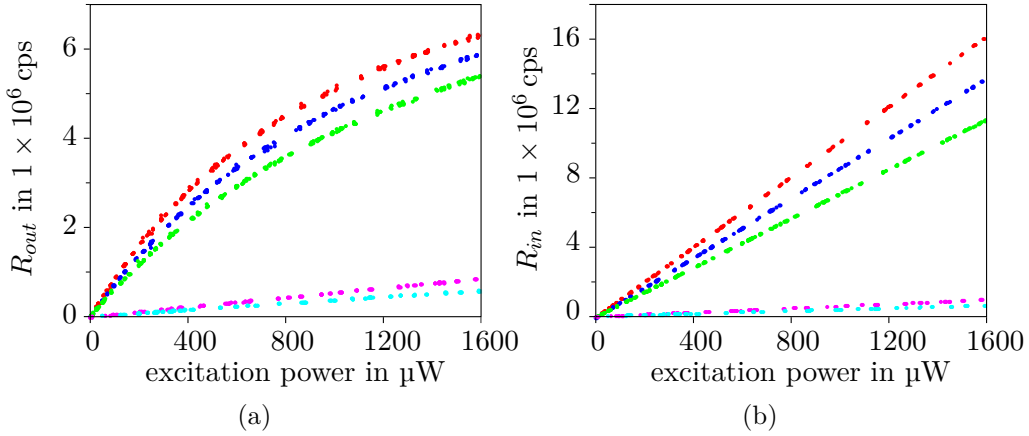


Figure A.1.: A laser, attenuated with different neutral filters, is shone on the APDs directly. The coloured plots indicate the data obtained using different neutral filters. In (a) the detection system's non-linear behaviour at high input rates is shown. (b) depicts the count rates corrected by means of the dead time correction in equation A.1.

Since the dead time of the whole detection system is not known, a statistical analysis is applied. The data are linearised by means of equation A.1 with a dead time τ_D for all being the same. Through varied dead times a value of 94 ns is evaluated, yielding accurate linear behaviour for all data curves (fig. A.1b). The constraint of the dead time correction, expressed in equation A.3, is met for all of our experimental data. This proves that the non-linearity truly arises from the dead time of the detection system.

The linearised count rates R_{in} are correlated to the measured rates R_{out} at the output of our detection system. The correlated pairs of count rates result in a calibration curve, shown in Figure A.2. On the x-axis, the count rate obtained via the detection system is plotted and the y-axis illustrates the dead time corrected count rates. The colours depict data obtained from measurements with different neutral filters which are in an exact alignment. In the case of small count rates the APDs work linear. This fact demands that the correction factor is 1, which is in agreement with our calibration curve.

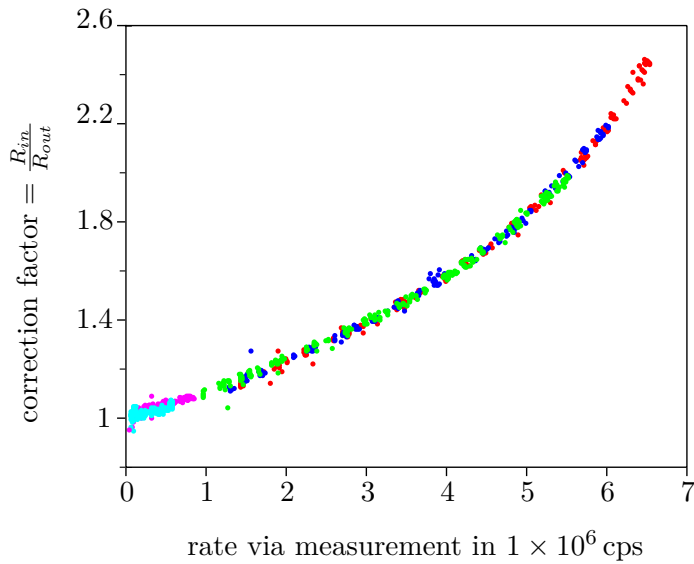


Figure A.2.: The calibration curve is received using the combination of the detection system's output rate R_{out} and the corresponding dead time corrected value R_{in} .

All measurements reporting absolute photon count rates are dead time corrected by a linear interpolation of this calibration curve. Note that for coincidence measurements using the **HBT** setup no such correction is applied.

Selbstständigkeitserklärung

Hiermit erkläre ich, Tanja Birgit Neumer, dass ich die vorliegende Arbeit allein und nur unter Verwendung deraufgeführten Quellen und Hilfsmittel angefertigt habe. Die Prüfungsordnung ist mir bekannt. Ich habe in meinem Studienfach bisher keine Masterarbeit eingereicht bzw. diese endgültig nicht bestanden.

Berlin, den
.....
(Tanja Birgit Neumer)

Bibliography

- [1] C. H. Bennett and G. Brassard. Quantum cryptography: Public key distribution and coin tossing. *Proceedings of IEEE International Conference on Computers, Systems, and Signal Processing*, 1984.
- [2] E. Knill, R. Laflamme, and G. J. Milburn. A scheme for efficient quantum computation with linear optics. *Nature*, 409:46–52, 2001.
- [3] F. Dolde, H. Fedder, M. W. Doherty, T. Nöbauer, F. Rempp, G. Balasubramanian, T. Wolf, F. Reinhard, L. C. L. Hollenberg, F. Jelezko, and J. Wrachtrup. Electric-field sensing using single diamond spins. *Nature Physics*, 7:459–463, 2011.
- [4] G. R. Guthöhrlein, M. Keller, K. Hayasaka, W. Lange, and H. Walther. A single ion as a nanoscopic probe of an optical field. *Nature*, 414:49–51, 2001.
- [5] M. Oxborrow and A. G. Sinclair. Single-photon sources. *Contemporary Physics*, 46(3):173–206, 2005.
- [6] G. S. Buller and R. J. Collins. Single-photon generation and detection. *Measurement Science and Technology*, 21(1):012002, 2010.
- [7] B. Lounis and M. Orrit. Single-photon sources. *Reports on Progress in Physics*, 68(5):1129, 2005.
- [8] C. K. Hong and L. Mandel. Experimental realization of a localized one-photon state. *Physical Review Letters*, 56:58–60, 1986.
- [9] H. Diedrich, F. and Walther. Nonclassical radiation of a single stored ion. *Physical Review Letters*, 58:203–206, 1987.
- [10] B. Darquié, M. P. A. Jones, J. Dingjan, J. Beugnon, S. Bergamini, Y. Sortais, G. Messin, A. Browaeys, and P. Grangier. Controlled single-photon emission from a single trapped two-level atom. *Science*, 309(5733):454–456, 2005.
- [11] W. E. Moerner. Single-photon sources based on single molecules in solids. *New Journal of Physics*, 6(1):88, 2004.
- [12] A. J. Shields. Semiconductor quantum light sources. *Nature Photonics*, 1(4):215–223, 2007.
- [13] V. Zwiller, T. Aichele, and O. Benson. Quantum optics with single quantum dot devices. *New Journal of Physics*, 6(1):96, 2004.
- [14] A. Högele, C. Galland, M. Winger, and Atac Imamoğlu. Photon antibunching in the photoluminescence spectra of a single carbon nanotube. *Physical Review Letters*, 100:217401, 2008.
- [15] I. Aharonovich, S. Castelletto, D. A. Simpson, C-H Su, A. D. Greentree, and S. Prawer. Diamond-based single-photon emitters. *Reports on Progress in Physics*, 74(7):076501, 2011.

Bibliography

- [16] C. Kurtsiefer, S. Mayer, P. Zarda, and H. Weinfurter. Stable solid-state source of single photons. *Physical Review Letters*, 85(2):290–293, 2000.
- [17] Oliver Benson. Assembly of hybrid photonic architectures from nanophotonic constituents. *Nature*, 480(7376):193–199, 2011.
- [18] Kerry J. Vahala. Optical microcavities. *Nature*, 424(6950):839–846, 2003.
- [19] D. Englund, B. Shields, K. Rivoire, F. Hatami, J. Vučković, H. Park, and M.D. Lukin. Deterministic coupling of a single nitrogen vacancy center to a photonic crystal cavity. *Nano Letters*, 10(10):3922–3926, 2010.
- [20] J. Wolters, G. Kewes, A. W. Schell, N. Nüsse, M. Schoengen, B. Löchel, T. Hanke, R. Bratschitsch, A. Leitenstorfer, T. Aichele, and O. Benson. Coupling of single nitrogen-vacancy defect centers in diamond nanocrystals to optical antennas and photonic crystal cavities. *Physica Status Solidi (b)*, 249(5):918–924, 2012.
- [21] J. T. Choy, B. J. M. Hausmann, T. M. Babinec, I. Bulu, M. Khan, P. Maletinsky, A.. Yacoby, and M. Lončar. Enhanced single-photon emission from a diamond-silver aperture. *Nature Photonics*, 5:738–743, 2011.
- [22] T. Schröder, F. Gädeke, M. J. Banholzer, and O. Benson. Ultrabright and efficient single-photon generation based on nitrogen-vacancy centres in nanodiamonds on a solid immersion lens. *New Journal of Physics*, 13(5):055017, 2011.
- [23] W.L. Barnes, G. Björk, J.M. Gérard, P. Jonsson, J.A.E. Wasey, P.T. Worthing, and V. Zwiller. Solid-state single photon sources: light collection strategies. *The European Physical Journal D*, 18:197–210, 2002. 10.1140/epjd/e20020024.
- [24] M. Deubel, G. von Freymann, M. Wegener, S. Pereira, K. Busch, and C. M. Soukoulis. Direct laser writing of three-dimensional photonic-crystal templates for telecommunications. *Nature Materials*, 3(7):444–447, 2004.
- [25] A. W. Schell, J. Kaschke, J. Fischer, R. Henze, J. Wolters, M. Wegener, and O. Benson. Three-dimensional quantum photonic elements based on single nitrogen vacancy-centres in laser-written microstructures. *Scientific Reports*, 3(1577), 2013.
- [26] T. Schröder, A. W. Schell, G. Kewes, T. Aichele, and O. Benson. Fiber-Integrated Diamond-Based Single Photon Source. *Nano Letters*, 2011.
- [27] R.J. Glauber. Coherent and incoherent states of the radiation field. *Physical Review*, 131:2766–2788, 1963.
- [28] M. O. Scully and M. S. Zubairy. *Quantum Optics*. Cambridge University Press, 1997.
- [29] R Loudon. Non-classical effects in the statistical properties of light. *Reports on Progress in Physics*, 43(7):913, 1980.
- [30] T. Aichele. *Detection and Generation of Non-Classical Light States from Single Quantum Emitters*. PhD thesis, Humboldt Universität zu Berlin, 2005.
- [31] A. Gruber, A. Dräbenstedt, C. Tietz, L. Fleury, J. Wrachtrup, and C. von Borczyskowski. Scanning confocal optical microscopy and magnetic resonance on single defect centers. *Science*, 276(5321):2012–2014, 1997.
- [32] M. W. Doherty, N. B. Manson, P. Delaney, F. Jelezko, J. Wrachtrup, and L. C. L. Hollenberg. The nitrogen-vacancy colour centre in diamond. *Physics Reports*, 528(1):1–45, 2013.

Bibliography

- [33] J. Walker. Optical absorption and luminescence in diamond. *Reports on Progress in Physics*, 42(10):1605, 1979.
- [34] A. M. Zaitsev. Vibronic spectra of impurity-related optical centers in diamond. *Physical Review B*, 61:12909–12922, 2000.
- [35] J. Tisler, G. Balasubramanian, B. Naydenov, R. Kolesov, B. Grotz, R. Reuter, J.-P. Boudou, P. A. Curmi, M. Sennour, A. Thorel, M. Börsch, K. Aulenbacher, R. Erdmann, P. R. Hemmer, F. Jelezko, and J. Wrachtrup. Fluorescence and spin properties of defects in single digit nanodiamonds. *ACS Nano*, 3(7):1959–1965, 2009.
- [36] Y. Mita. Change of absorption spectra in type-ib diamond with heavy neutron irradiation. *Physical Review B*, 53:11360–11364, 1996.
- [37] J. H. N. Loubser and J. A. van Wyk. Electron spin resonance in the study of diamond. *Reports on Progress in Physics*, 41(8):1201, 1978.
- [38] T. Gaebel, M. Domhan, C. Wittmann, I. Popa, F. Jelezko, J. Rabeau, A. Greentree, S. Prawer, E. Trajkov, P. R. Hemmer, and J. Wrachtrup. Photochromism in single nitrogen-vacancy defect in diamond. *Applied Physics B*, 82(2):243–246, 2006.
- [39] A. Gali. Theory of the neutral nitrogen-vacancy center in diamond and its application to the realization of a qubit. *Physical Review B*, 79:235210, 2009.
- [40] P. Tamarat, N. B. Manson, J. P. Harrison, R. L. McMurtrie, A Nizovtsev, C. Santori, R. G. Beausoleil, P. Neumann, T. Gaebel, F. Jelezko, P. Hemmer, and J. Wrachtrup. Spin-flip and spin-conserving optical transitions of the nitrogen-vacancy centre in diamond. *New Journal of Physics*, 10(4):045004, 2008.
- [41] A. Batalov, V. Jacques, F. Kaiser, P. Siyushev, P. Neumann, L. J. Rogers, R. L. McMurtrie, N. B. Manson, F. Jelezko, and J. Wrachtrup. Low temperature studies of the excited-state structure of negatively charged nitrogen-vacancy color centers in diamond. *Physical Review Letters*, 102:195506, 2009.
- [42] L. J. Rogers, S. Armstrong, M. J. Sellars, and N. B. Manson. Infrared emission of the nv centre in diamond: Zeeman and uniaxial stress studies. *New Journal of Physics*, 10(10):103024, 2008.
- [43] M. W. Doherty, F. Dolde, H. Fedder, F. Jelezko, J. Wrachtrup, N. B. Manson, and L. C. L. Hollenberg. Theory of the ground-state spin of the nv^- center in diamond. *Physical Review B*, 85(20):205203, 2012.
- [44] G. Davies. The effect of nitrogen impurity on the annealing of radiation damage in diamond. *Journal of Physics C: Solid State Physics*, 5(17):2534, 1972.
- [45] J. E. Ralph. Radiation induced changes in the cathodoluminescence spectra of natural diamonds. *Proceedings of the Physical Society*, 76(5):688, 1960.
- [46] H. B. Dyer and L. du Preez. Irradiation damage in type i diamond. *The Journal of Chemical Physics*, 42(6):1898–1906, 1965.
- [47] C. D. Clark and C. A. Norris. Photoluminescence associated with the 1.673, 1.944 and 2.498 ev centres in diamond. *Journal of Physics C: Solid State Physics*, 4(14):2223, 1971.

Bibliography

- [48] J. Wolters, N. Sadzak, A. W. Schell, T. Schröder, and O. Benson. Measurement of the ultrafast spectral diffusion of the optical transition of nitrogen vacancy centers in nano-size diamond using correlation interferometry. *Physical Review Letters*, 110:027401, 2013.
- [49] A. Beveratos, R. Brouri, T. Gacoin, J. P. Poizat, and P. Grangier. Nonclassical radiation from diamond nanocrystals. *Physical Review A*, 64(6):061802, 2001.
- [50] J. P. Hadden, J. P. Harrison, A. C. Stanley-Clarke, L. Marseglia, Y.-L. D. Ho, B. R. Patton, J. L. O'Brien, and J. G. Rarity. Strongly enhanced photon collection from diamond defect centers under microfabricated integrated solid immersion lenses. *Applied Physics Letters*, 97:241901–1 – 241901–3, 2010.
- [51] P. Siyushev, F. Kaiser, V. Jacques, I. Gerhardt, S. Bischof, H. Fedder, J. Dodson, M. Markham, D. Twitchen, F. Jelezko, and J. Wrachtrup. Monolithic diamond optics for single photon detection. *Applied Physics Letters*, 97:241902, 2010.
- [52] L. Marseglia, J. P. Hadden, A. C. Stanley-Clarke, J. P. Harrison, B. Patton, Y.-L. D. Ho, B. Naydenov, F. Jelezko, J. Meijer, P. R. Dolan, J. M. Smith, J. G. Rarity, and J. L. O'Brien. Nanofabricated solid immersion lenses registered to single emitters in diamond. *Applied Physics Letters*, 98, 2011.
- [53] T. M. Babinec, B. J. M. Hausmann, M. Khan, Y. Zhang, J. R. Maze, P. R. Hemmer, and M. Lončar. A diamond nanowire single-photon source. *Nature Nanotechnology*, 5:195 – 199, 2010.
- [54] A. Mohtashami and A. F. Koenderink. Suitability of nanodiamond nitrogen-vacancy centers for spontaneous emission control experiments. *New Journal of Physics*, 15(4):043017, 2013.
- [55] L. Liebermeister, F. Petersen, A. v. Münchow, D. Burchardt, J. Hermelbracht, T. Tashima, A. W. Schell, O. Benson, T. Meinhardt, A. Krueger, A. Stiebeiner, A. Rauschenbeutel, H. Weinfurter, and M. Weber. Tapered fiber coupling of single photons emitted by a deterministically positioned single nitrogen vacancy center. *Applied Physics Letters*, 104(3):–, 2014.
- [56] E. Ampem-Lassen, D. A. Simpson, B. C. Gibson, S. Trpkovski, F. M. Hossain, S. T. Huntington, K. Ganesan, L. C. Hollenberg, and S. Prawer. Nano-manipulation of diamond-based single photon sources. *Optical Express*, 17(14):11287–11293, 2009.
- [57] L. Novotny and B. Hecht. *Principles of Nano-Optics*. Cambridge University Press, 2006.
- [58] J. Fischer and M. Wegener. Three-dimensional optical laser lithography beyond the diffraction limit. *Laser and Photonics Reviews*, 7(1):22–44, 2013.
- [59] F. Klein, T. Striebel, J. Fischer, Z. Jiang, C. M. Franz, G. von Freymann, M. Wegener, and M. Bastmeyer. Elastic fully three-dimensional microstructure scaffolds for cell force measurements. *Advanced Materials*, 22(8):868–871, 2010.
- [60] M. Thiel, J. Fischer, G. von Freymann, and M. Wegener. Direct laser writing of three-dimensional submicron structures using a continuous-wave laser at 532 nm. *Applied Physics Letters*, 97(22), 2010.
- [61] R. H. Webb. Confocal optical microscopy. *Reports on Progress in Physics*, 59(3):427, 1996.

Bibliography

- [62] G. A. Steudle, S. Schietinger, D. Höckel, S. N. Dorenbos, I. E. Zadeh, V. Zwiller, and O. Benson. Measuring the quantum nature of light with a single source and a single detector. *Physical Review A*, 86:053814, 2012.
- [63] R. Hanbury Brown and R. Q. Twiss. Correlation between photons in two coherent beams of light. *Nature*, 177(17):27–29, 1956.
- [64] J.W. Goodman. *Introduction to Fourier Optics*. Roberts & Company, 2005.
- [65] B. E. A. Saleh and M. C. Teich. *Fundamentals of Photonics*. John Wiley, 1991.
- [66] PerkinElmer Optoelectronics. *SPCM-AQR, Single Photon Counting Module, data sheet*.
- [67] W. P. Ambrose, Th. Basché, and W. E. Moerner. Detection and spectroscopy of single pentacene molecules in a p-terphenyl crystal by means of fluorescence excitation. *The Journal of Chemical Physics*, 95(10):7150–7163, 1991.
- [68] L. Fleury, Ph. Tamarat, B. Lounis, J. Bernard, and M. Orrit. Fluorescence spectra of single pentacene molecules in p-terphenyl at 1.7 k. *Chemical Physics Letters*, 236(1-2):87 – 95, 1995.
- [69] A. Drechsler, M. Lieb, C. Debus, Alfred Meixner, and G. Tarrach. Confocal microscopy with a high numerical aperture parabolic mirror. *Optical Express*, 9(12):637–644, 2001.
- [70] N. Davidson and N. Bokor. High-numerical-aperture focusing of radially polarized-doughnut beams with a parabolic mirror and a flat diffractivelens. *Optical Letters*, 29(12):1318–1320, 2004.
- [71] J. Stadler, C. Stanciu, C. Stupperich, and A. J. Meixner. Tighter focusing with a parabolic mirror. *Optical Letters*, 33(7):681–683, 2008.
- [72] E. H. Chen, O. Gaathon, M. E. Trusheim, and D. Englund. Wide-field multispectral super-resolution imaging using spin-dependent fluorescence in nanodiamonds. *Nano Letters*, 13(5):2073–2077, 2013.
- [73] W. L. Barnes. Fluorescence near interfaces: The role of photonic mode density. *Journal of Modern Optics*, 45(4):661–699, 1998.
- [74] W. Lukosz. Light emission by magnetic and electric dipoles close to a plane dielectric interface. iii. radiation patterns of dipoles with arbitrary orientation. *Journal of the Optical Society of America*, 69(11):1495–1503, 1979.
- [75] S. Kawata, H. B. Sun, T. Tanaka, and K. Takada. Finer features for functional microdevices. *Nature*, 412(6848):697–698, 2001.
- [76] J. D. Jackson. *Classical Electrodynamics*. John Wiley, 1999.
- [77] K. Yee. Numerical solution of initial boundary value problems involving maxwell's equations in isotropic media. *IEEE Transactions on Antennas and Propagation*, 14(3):302–307, 1966.
- [78] A. Taflove and S. C. Hagness. *Computational electrodynamics: the finite-difference time-domain method*. Artech House, 3rd edition, 2005.
- [79] S. M. Mansfield and G. S. Kino. Solid immersion microscope. *Applied Physics Letters*, 57(24):2615–2616, 1990.

Bibliography

- [80] V. Zwiller and G. Bjork. Improved light extraction from emitters in high refractive index materials using solid immersion lenses. *Journal of Applied Physics*, 92(2):660–665, 2002.
- [81] W. Lukosz and R. E. Kunz. Light emission by magnetic and electric dipoles close to a plane interface. i. total radiated power. *Journal of the Optical Society of America*, 67(12):1607–1615, 1977.
- [82] R. Winston, W. T. Welford, J. C. Mi  nano, and P. Ben  itez. *Nonimaging Optics*. Elsevier Academic Press, 2005.
- [83] C. Meeks and P. B. Siegel. Dead time correction via the time series. *American Journal of Physics*, 76(6):589–590, 2008.
- [84] R. L. Lucke. Counting statistics for nonnegligible dead time corrections. *Review of Scientific Instruments*, 47(6):766–767, 1976.